

Intrinsic Absorption Properties in Active Galaxies Observed with the Far Ultraviolet Spectroscopic Explorer¹

Jay P. Dunn², D. Michael Crenshaw², S. B. Kraemer³, & M. L. Trippe²

ABSTRACT

In a continuing survey of active galactic nuclei observed by the *Far Ultraviolet Spectroscopic Explorer*, we provide a deeper analysis of intrinsic absorption features found in 35 objects. Our survey is for low-redshift and moderate-luminosity objects, mostly Seyfert galaxies. We find a strong correlation between maximum radial velocity and luminosity. We also examine the relationships between equivalent width (EW), full width at half maximum, velocity and continuum flux. The correlation between velocity and luminosity has been explored previously by Laor & Brandt, but at a significantly higher redshift and heavily weighted by broad absorption line quasars. We also have examined each object with multiple observations for variability in each of the aforementioned quantities, and have characterized the variation of EW with the continuum flux. In our survey, we find that variability of O VI $\lambda\lambda 1032, 1038$ is less common than of the UV doublets of C IV and N V seen at longer wavelengths, because the O VI absorption is usually saturated. Lyman β absorption variability is more frequent. In a target-by-target examination we find that broad absorption line and narrow absorption line absorbers are related in terms of maximum outflow velocity and luminosity, and both can be exhibited in similar luminosity objects. We also find one object that shows radial velocity change, seven objects that show equivalent width variability and two objects that show either transverse velocity changes or a change in ionization.

Subject headings: galaxies: Seyfert – ultraviolet: galaxies

¹Based on observations made with the NASA-CNES-CSA Far Ultraviolet Spectroscopic Explorer. *FUSE* is operated for NASA by the Johns Hopkins University under NASA contract NAS5-32985.

²Department of Physics and Astronomy, Georgia State University, Atlanta, GA 30303. Email: dunn@chara.gsu.edu, crenshaw@chara.gsu.edu, trippe@chara.gsu.edu

³Institute for Astrophysics and Computational Sciences, Department of Physics, The Catholic University of America, Washington, DC 20064; kraemer@yancey.gsfc.nasa.gov.

1. Introduction

It is commonly known that intrinsic UV absorption occurs in a large fraction ($\sim 50\%$) of Seyfert galaxies. First noticed by Anderson & Kraft (1969), several surveys have been done in recent years (Crenshaw et al. 1999; Kriss 2002; and Dunn et al. 2007, hereafter Paper I) to characterize these features. In the first step of our survey we examined low- z active galactic nuclei (AGN) (Paper I). Seyfert galaxies are moderately luminous, relatively nearby, and mostly spiral galaxies, which make up a large portion of our survey, while the remainder are low-redshift quasars. We concentrate only on AGN that show broad permitted emission lines and narrow emission lines (i.e., Seyfert 1’s, Kachikian & Weedman 1974). This is because intrinsic absorption is only readily detectable if seen against the broad emission lines and central continuum source characteristic of type 1 objects. Seyfert 2 galaxies have only narrow permitted and forbidden lines, and thus intrinsic absorption cannot be easily detected.

Crenshaw et al. (1999) performed a survey of Seyfert galaxies that had been observed with the Faint Object Spectrograph (FOS) and investigated the properties of the intrinsic absorption lines. They found that nearly 60% of the targets in the survey showed narrow C IV absorption features ($\text{FWHM} < 500 \text{ km s}^{-1}$) and outflow velocities up to 2000 km s^{-1} . Also in this survey, they found a link between warm X-Ray absorbers and UV intrinsic absorption, in the sense that Seyfert galaxies that show one also show the other.

Broad absorption line (BAL) quasars have been studied even more extensively. These objects show lines with much larger velocity widths, up to $\sim 10,000 \text{ km s}^{-1}$ (Weymann et al. 1981, Turnshek 1988), which appear in $\sim 10\%$ of all quasars (Foltz et al. 1990). This is a much smaller percentage than the percentage that exhibit narrow absorption lines only, so the global covering factor is an important consideration in determining their nature.

Laor & Brandt (2002) looked for various trends concerning intrinsic absorption in data from the *Hubble Space Telescope (HST)* and the *International Ultraviolet Explorer (IUE)*. Their survey was derived from the PG quasar sample (Boroson & Green 1992). One of the more notable trends they found was a dependence of maximum outflow velocity on luminosity ($v_{max} \propto L^{0.62 \pm 0.08}$). Their plot contains both BAL and narrow absorption lines (NALs). They found that the equivalent width (EW) also followed an increase with increasing luminosity. This trend is based on Soft X-Ray Weak Quasars (SXWQs), which show larger values of EW and v_{max} than any other quasar across the luminosity span. They furthermore showed that [O III] EW and v_{max} are correlated. SXWQs showed a significant correlation of EW versus v_{max} . Of the 56 objects they investigated, 28 showed intrinsic UV absorption. This agrees well with the $\sim 60\%$ frequency Crenshaw et al. (1999) found in their lower-luminosity sample and the $\sim 50\%$ frequency we found in Paper I.

For a purely BAL sample, Ganguly et al. (2007) recently used data from the Sloan Digital Sky Survey (SDSS) to investigate their properties. They conclude that the overall fit between v_{max} and luminosity found by Laor & Brandt applies to their much larger sample of over 5000 objects. In Ganguly & Brotherton (2008), they compile all intrinsic absorption features for all known surveys and show that the fit still holds.

Our knowledge of the variability for intrinsic absorption is limited. Variability is important because it is our only link to several key physical parameters concerning the AGN. Cromwell & Weymann (1970) were the first to detect variability, in the Seyfert 1 NGC 4151. Later, in data from the *IUE*, more absorption variability was seen (Crenshaw et al. 1999). Nearly all of the variability has been due to changes in the ionic column densities, as a result of changes in the ionizing flux from the continuum source. However, in four Seyfert galaxies (NGC 3516, NGC 3783, NGC 4151, and NGC 5548), bulk transverse motion of gas across the line of sight was identified as a likely culprit (Crenshaw et al. 2003). In the bright Seyfert galaxy NGC 4151, both ionization change and bulk transverse motion were detected. Kraemer et al. (2006) performed a detailed analysis of the absorption from the Space Telescope Imaging Spectrograph (STIS) data. For the component they dubbed D+Ed, they found a transverse velocity lower limit of $v_t \geq 2100 \text{ km s}^{-1}$.

NGC 3783 has shown previously to be variable (Gabel et al. 2005, Maran et al. 1996). In 1993 February data from STIS, NGC 3783 showed a spectrum with no narrow intrinsic absorption. By 1994 January, two obvious absorption features arose for each member of the C IV doublet. By 2000 February another pair of absorption lines had emerged. Gabel et al. (2003) showed that the radial velocity changed as well. In a series of several spectra the radial velocity of the line changed in two time spans. They first found a change of $\sim 35 \text{ km s}^{-1}$ and in the second span they saw a change of $\sim 55 \text{ km s}^{-1}$. This is the first well-documented case of a change in radial velocity for an intrinsic absorber in a Seyfert galaxy. Transverse velocity was also measurable, where they found a lower limit of $v_t \geq 540 \text{ km s}^{-1}$, which is comparable to the radial velocity ($\sim -450 \text{ km s}^{-1}$). Motivated by their findings, we undertook a survey of O VI and Ly β absorption in *Far Ultraviolet Spectroscopic Explorer* (*FUSE*) spectra of low-redshift AGN.

The penultimate goal of our research is to understand the general dynamics of mass outflow and to ultimately help complete the picture of the AGN central engine. Several dynamical scenarios have been offered as explanations for the outflow (see Crenshaw et al. 2003 for a review of the models). One method, Compton heated winds assumes that EUV and X-ray photons from the accretion disk are irradiating the gas at larger distances and creating a thermal wind (Begelman et al. 1983). Radiative driving is also a promising method to explain fast-moving outflows such as BALs (deKool & Begelman 1995, Arav et

al. 1994). Another possibility is that magnetic fields from the accretion disk are lifting plasma from the disk in magnetohydrodynamic (MHD) flows, where the plasma follows a helical magnetic field line (Blandford & Payne 1982). Depending on how far from the central core these clouds can follow the field lines, this could also be an explanation for the high transverse velocities.

In Paper I we cataloged 35 AGN with intrinsic absorption and presented approximate velocities. We found 11 new UV intrinsic absorption objects in a sample of 90 nearby AGN observed by *FUSE*. We calculated the frequency of O VI absorption to be on the order of 50%, slightly lower than the value Crenshaw et al. (1999) found for C IV. The global covering factor, based on an estimate of the average covering factor in the line of sight ($\langle C_f \rangle$) was similar to previous results of ~ 0.4 . We continue our study of that absorption measurements of the absorption lines we found in the 35 objects from Paper I.

2. Optical Observations and Measurements

We obtained ground-based optical spectra to obtain redshifts and/or estimate black-hole masses and to supplement the *FUSE* data for three objects: IRAS F22456-5125, MR 2251-178 and WPVS 007. These data are readily available in the literature for most of the other objects. Each galaxy was observed in both the blue and red optical regions with the R-C spectrograph on the Cerro Tololo Inter-American Observatory (CTIO) 1.5-m telescope in Chile. Table 1 chronicles the dates, integration times and wavelength coverage for these data. The blue spectra (spanning from approximately 3360 to 5440 Å) were taken using a grating with a dispersion of $\sim 1.47 \text{ \AA pixel}^{-1}$, providing a resolution of 4.3 Å. The red spectra (5652 to 6972 Å) were taken using a Schott GG495 filter and a grating with a $1.10 \text{ \AA pixel}^{-1}$ dispersion grating giving us a resolution of 3.1 Å. All objects were observed through a long slit with a width of 4". The stars LTT 4364 and Feige 110 were observed with the same settings for the purpose of flux calibration. The spectra were reduced and calibrated using standard IRAF reduction packages for long-slit spectroscopy. We show the reduced spectra in Figure 1.

For the source IRAS F22456-5125, which had a redshift estimate listed on NASA/IPAC Extragalactic Database (NED) of 0.1 (Mason et al. 1995), we used our spectra to estimate the redshift based on the positions of lines in the blue spectrum. The centroids of the emission lines [O II] $\lambda 3727$, [Ne III] $\lambda 3869$, [Ne V] $\lambda 3424$ and $H\beta$ were available in the wavelength coverage of the blue setting and we found an average redshift of $z=0.1016 \pm 0.0001$. The redshifts from NED for WPVS 007 and MR-2251-178 are consistent with our measurements.

The optical spectra allowed us to determine mass estimates for the central supermassive black hole (SMBH) of these objects via the empirical relationships between SMBH mass and the $H\beta$ FWHM and continuum luminosity at $\lambda=5100\text{\AA}$ (or, equivalently the $H\beta$ line luminosity) calibrated by Vestergaard and Peterson (2006) using emission-line reverberation mapping. We present these masses along with the masses of the rest of the sample later in this paper.

3. UV Observations and Measurement

We have 105 observations from *FUSE* of the 35 targets found with intrinsic absorption from Paper I (see Table 1 from Paper I). *FUSE* consists of four telescopes each with four gratings and two detectors with a spectral resolution of $\sim 15 \text{ km s}^{-1}$, which provides 8 spectra per observation covering the wavelength range of 905 \AA to 1187 \AA . The detectors have two different coatings, LiF and SiC. The detector with the LiF coating provides a (nearly twice) higher reflectivity than the SiC coating (Sahnou 2002). The SiC and LiF detectors do have overlapping regions that allow for the spectra to be coadded, weighted by exposure time, and scaled to the LiF 1a spectrum. We downloaded the spectra from MAST and used CalFUSE 3.1 to process the raw data in time-tag mode (Dixon et al. 2002). Further details of the reduction process can be found in Paper I.

3.1. Light Curves

Generating a continuum light curve for *FUSE* data proved to be a difficult task due to the nature of the two detectors and redshifted broad emission lines. Using the same method as described by Dunn et al. (2006), we chose 1110 \AA in the observed frame as a good position to measure the continuum flux. In a 10 \AA bin, both detectors contribute to the measured flux at that wavelength. In some spectra from either the LiF detector or the SiC detector, the target was sometimes out of the aperture. In these cases we did not include the segments. Also, due to redshift considerations, we were forced to move the bin when the redshift was ≥ 0.6 . At those particular redshifts the broad line would provide a measured flux value too high for the continuum by up to 20-30%. For the majority of the observations, the flux we provide is an average flux within the 10 \AA bin at 1110 \AA ; this avoids interstellar medium (ISM) lines (Morton 1991) and geocoronal dayglow lines (Feldman et al. 2001). The rest of the observations were measured in a 20 \AA bin taken at 1160 or 1020 \AA , depending on which was closest to and unobstructed by the O VI broad line. We converted our fluxes to log specific luminosity, and provide flux, log luminosity, bin position, and errors in Table 2.

3.2. Measured Absorption Quantities

We measured the EW, full width at half-maximum (FWHM) and radial velocity centroid with respect to systemic redshift of each intrinsic absorption feature identified in Paper I. These measurements are listed in Table 3 for the Ly β , O VI λ 1032 (O VIb) and O VI λ 1038 (O VIr) lines. Many features were blended or too contaminated by galactic absorption features to be measured accurately, thus they have been excluded. Because *FUSE* has no onboard calibration lamp, CalFUSE is designed to apply a fit to the spectrum based on a predetermined wavelength solution (Sahnou 2000). This can lead to an inaccuracy of up to 20 km s $^{-1}$ (Gillmon et al. 2006). We measured available ISM lines near our intrinsic absorption features, in order to avoid nonlinear calibration effects, to correct the velocities. These corrections have already been accounted for in our velocities in Table 3.

Errors for EWs were based upon the signal-to-noise (S/N) ratio of the data along with the standard deviation of three measurements of each line with three different continuum estimates. The quoted error is a sum of these two values. Because velocity centroids, which are depth weighted, have small standard deviation errors for one line, we used the mean standard deviation for the three lines (Ly β , O VIb, O VIr) in each observation. For FWHM we estimated the error as the standard deviation of the three measurements per line, similar to EW.

We estimated flux error from the standard deviation within the 10 or 20 Å bin. This is typically an overestimate of the error due to oversampling, similar to the case for IUE data (Dunn et al. 2006). We find that we overestimate by nearly a factor of 2.5 by examining spectra close in time (\lesssim 1 day) for like objects. Because most of these objects are Seyfert galaxies, the flux level is not likely to change significantly in the span of \lesssim 1 day. We therefore scaled our flux errors by this amount.

Our listed redshifts for the objects are provided by NED. We chose them based on the recommended most accurate value, preferably from HI-21 cm measurements. However, not all objects have very accurate values for the redshift, such as IRASF 22456-5125 (ϕ 2). Some of the redshifts are from narrow emission lines, which are often blue shifted with respect to HI-21 cm values (Crenshaw et al. 1999). This may explain the slightly positive radial velocities found for some components in a few objects.

In several cases we found that of the three lines we examined, only one or two of the lines were measurable. This is due to either poor signal-to-noise, Ly β being too weak, or heavy blending with ISM features.

4. Correlations

All of our correlations involving EW, FWHM and/or luminosity show measurements from each absorption component in each observation, because many of these quantities can be variable over time. In order to inspect our plots for correlations we simply examine by eye the data for either a direct trend or for an envelope fit to the data, as in Laor & Brandt (2002).

The plots containing velocity measurements are averaged over time due to the lack of significant variability in velocity space. Also, error bars for many of the points are contained within the plot symbol. The most tantalizing correlation we have found is that of velocity with luminosity. While this was seen in C IV by Laor & Brandt (2002), their objects were mostly quasars with high luminosities and redshifts beyond 1.5, which was our redshift cutoff on the high end. We share four objects in common. We plot in Figure 2 all of our velocities measured for each object and each component. In general as the luminosity increases, it appears that the maximum velocity at each luminosity does as well. This confirms the trend that Laor & Brandt found for higher-luminosity objects and shows that the trend also holds for lower-luminosity objects such as Seyfert galaxies. To confirm this further, we converted the magnitudes provided by Laor & Brandt to $\log L_\lambda$ by using the four targets we share and found a scale factor of 1.7. We plot the Laor & Brandt observations along with our own measurements in Figure 3 and see that the two data sets follow remarkably similar trends. The relation given by Laor & Brandt is $v_{max} \propto L^{0.62 \pm 0.08}$. While we do not calculate this, we can see by Figure 3 that all of our points fall beneath this maximum velocity trend.

Ganguly & Brotherton (2008) show a similar plot. They have plotted the Laor & Brandt (2002) data along with their SDSS data from Ganguly et al. (2007), and data from several other sources (references within). The plot shows that for all available data the trend from Laor & Brandt holds for all luminosities and velocities.

Along with the measured black hole-masses from the optical data, we compiled all of the known masses for our survey objects in Table 4 (we exclude those few without the necessary measured quantities) and calculated the Eddington ratio. For all objects referencing Peterson et al. (2004), the masses are from reverberation mapping; all others were calculated using the relationship found by Kaspi et al. 2000 and calibrated by Vestergaard & Peterson (2006):

$$M_{BH} = \log \left[\left(\frac{FWHM(H\beta)}{1000 \text{ km s}^{-1}} \right)^2 \left(\frac{\lambda L_{5100}}{10^{43} \text{ ergs s}^{-1}} \right)^{0.5} \right] \quad (1)$$

using the FWHM of the broad $H\beta$ emission line and the luminosity at 5100 Å. We find our value for $L_{Bol} = 9.8 \lambda L_{5100}$ from McLure & Dunlop (2004).

We plot the maximum velocity, as before with luminosity, against the Eddington ratio (L/L_{Edd}) in Figure 4. There appears to be a weak trend of maximum velocity with the Eddington ratio. It should be noted that the two objects with the highest velocities have low ratios, and the two objects with a high ratio have low velocities. In order to complete the picture we would require more data and a wider range of objects spanning the range of ratios as most of our targets are moderate Eddington accreting objects.

We examined how the EW relates to the specific luminosity in our sample, which we show in Figure 5. Overall there appears to be no trend. This contradicts the findings of Laor & Brandt (2002) for C IV lines, but this could be a simple case of saturation affecting our EW measurements. The only notable feature in the plot is the lack of points for low luminosity and low EW. The paucity of points is most likely a selection effect of low signal-to-noise for weak lines in objects with low-continuum fluxes. It should be noted that, some of our measured EWs are measured over what have been seen, in less saturated UV absorption lines, to be multiple components (e.g., NGC 4151 in Kraemer et al. 2005). Due to the heavy blending and saturation in O VI, we simply measure across blends as one component. We have removed any measurements of lines in spectra with a luminosity signal-to-noise of < 30 and measurements from spectra that are saturated with multiple components, and still find that there is no trend.

We additionally investigated the relation between EW and maximum velocity (not shown). Again, there appears to be very little trend. We also examined the relation between FWHM and the specific luminosity, as shown in Figure 6. There appears to be no relation between FWHM and luminosity. However, as seen with EW, there does appear to be a lack of absorption for O VI at low luminosities and small FWHMs.

5. Variability

Our survey is the first to date with a significant number of objects with multiple spectra to provide enough data for a time series analysis of intrinsic absorption variability in the far ultraviolet. Of the 35 targets found in the Paper I survey, 22 of the objects have multiple observations. Using the EWs, velocities and FWHMs we provided in Table 3, we examined a time series of each along with the corresponding fluxes for each observation from Table 2. Along with the times series data, we plotted the spectra for each object in chronological order to see visually how the absorption features changed. While most objects showed no real trends between EW, FWHM, or velocity vs. continuum flux, we found a handful of cases that do.

Mrk 79 is one case of a likely variation. $\text{Ly}\beta$ is clearly visible in the observations in Figure 7. Component 1 of O VIb is a broad feature due to blending with ISM lines. O VIr is a narrow, most likely saturated line. The variability for Mrk 79 is seen in the O VIr line. O VIr changes in EW for component 1, but does not appear to be correlated with continuum luminosity in Figure 8.

NGC 4151 has broad, saturated absorption troughs. These troughs are comprised of several blended components seen as individual features in STIS data (Kraemer et al. 2001). Because they are blended, it makes measuring individual EWs, FWHMs and velocities difficult. One interesting point is that in the first two observations, seen in Figure 9, the broad trough shows some structure, but in the subsequent observations, they blend too much to discern any one particular absorber. As shown in Kraemer et al. (2001), one particular component, labeled D', only appears in weak flux states. In Table 2 we see that the earlier observations are weaker in flux, and that the D' component flattens the region between ~ 1029 and 1032 \AA , which is consistent with the interpretation of Kraemer et al.

Mrk 817 is another object that shows evidence of variability. One of the labels in Dunn et al. (2007) is incorrect; the Lyman β line is weak, and the line marked component 1 at 1064 \AA is H_2 . In Figure 10, we see that Mrk 817 shows in O VIb that component 1 evolves from two subcomponents to a smoother single component. It is possible that these subcomponents are hidden within the artificially broadened O VIr line due to galactic Fe II $\lambda 1055$. Lyman β is not visible most likely due to high ionization. This is confirmed by STIS spectra that show weak absorption in Lyman α (Penton, Stocke & Shull 2002). The EW for the original lines shows a correlation with the decreasing continuum flux (Figure 11), and FWHM shows the same. While this is a 2σ detection in O VIb, the similar behavior of all three lines leads us to believe that the change is real. The velocity seems to drop for Mrk 817 showing a significant decrease between the first observation and the last. All of this suggests two blended components in the original observation, and that the higher-velocity component decreased with time.

Mrk 817 also demonstrates the appearance of a previously unseen line. At $\sim 1052 \text{ \AA}$ and $\sim 1058 \text{ \AA}$ we see that in the first spectrum there is no significant sign of an absorption feature. However in the third spectrum there appears to be a slightly depressed broad feature, and in the final spectrum the broad line is clear with two O VI features on either side at the appropriate locations in velocity space $v_r=3700$ & 3430 km s^{-1} . However, we cannot rule out the possibility that the new component is present in the previous observations but not detectable due to the lower S/N.

In Figure 12, we present the available spectra for Mrk 279. Figure 13 shows the relation of EW and continuum flux for Mrk 279, which shows a weak trend. In both O VI lines

the EW increases with decreasing flux. For Ly β the relationship with flux is much flatter. During the last three observations we see the flux drop by $\sim 60\%$ and then increase by $\sim 50\%$, while the EW for all three lines shows a chronological decrease. We see that O VIb varies more than O VIr in Mrk 279. This is most likely due to contamination in both of the O VI lines from ISM and H₂. While these lines are heavily contaminated (see Paper I), we can still measure variation as the ISM lines should experience no change.

Mrk 290 (Figure 14) provides a case for a weak anti-correlation between EW and flux. In this object the EWs for both members of the O VI doublet $\lambda\lambda$ 1032 and 1038 lines show a slight decrease with a significant increase in continuum flux over a 1200 day interval, and a moderate decrease in the Ly β width, as shown in Figure 15.

The variability in Mrk 509 was complex, as shown in Figure 16. What we measured for component 1, can be seen in Lyman β to be at least two subcomponents in two of our three spectra. What we call component 2 can be seen in Lyman β to be comprised of at least two or three subcomponents. Kraemer et al. (2003) confirm this by identifying 8 components in spectra from FOS and STIS, which are blended together with the two main components we see in the *FUSE* data. The components labeled 1-3 by Kraemer et al. are subcomponents that are contained in our measured component 1, while those labeled 4-8 by Kraemer et al. make up our measured component 2. Subcomponents 3 and 6 in Lyman β , labeled by Kraemer et al. appear to vary. Subcomponent 3 shows an decrease in depth while subcomponent 6 increases in depth over time. We discuss the depth further in the next section. Our measured component 1 shows no change in EW or velocity over time (Figure 17), but our measured component 2 shows a slight increase in Ly β (Figure 18).

Figure 19 shows the spectra of PG 0804+761, which exhibits evidence of radial velocity change. This change is seen in all three lines as a centroid shift to more negative velocities, while the ISM lines remain stationary. We plot these centroid velocities vs. time (Figure 20). PG 0804+761 has a poor estimate of redshift, similar to IRAS F22456-5125. Thus the absolute values of velocity reflect redshifted lines, but this might change with a more accurate redshift.

In the object NGC 3783, we find variability of EW in the Ly β line. Figure 21 shows the time evolution of the spectrum, and Figure 22 shows the relation between flux and EW and velocity over time. The EWs for O VI λ 1038 and O VI λ 1032 show no correlation, across the dashed average EW line. Ly β decreases from low flux to high flux. However, this is evidently a blended combination of two lines labeled 2 and 3 in a paper by Gabel et al. (2003). Thus it is difficult to determine if one or both lines are responding to continuum change. In Figure 21, we see that components 1 and 4 from Gabel et al. (2003) are visible in Ly β , and are hard to discern in O VI λ 1032 due to heavy contamination from C II and

H₂. For O VI λ 1038 there are two H₂ lines nearby, but the weak component 4 is not visible.

6. Discussion

In the Kraemer et al. (2005, 2006) study of the variability in NGC 4151, they found some cases where the EWs of lines were anti-correlated with the continuum flux level, while others showed no relation to the flux. We see similar events in only a few objects such as Mrk 817, where the O VI lines seem to follow the continuum, and Mrk 79, where the EWs vary but the continuum stays relatively constant. The paucity of O VI variability suggests that O VI, which is usually predicted to be very strong in absorber models, is saturated in most cases. It should also be noted that in many cases there is a lack of change in $Ly\beta$, this is presumably also due to saturation. The changes we do see in EW must be due to one of the three events: a covering factor change in the line of sight, a change in ionization, or a total column change (characterized by N_H) due for example, to bulk motion of gas into our line of sight.

6.1. Potential Cases of Bulk Motion

There are three targets in our survey that show changes in the absorption are the best candidates for bulk motion of gas across the line of sight with a transverse velocity (v_t), as described below. These three objects are Mrk 79, Mrk 817 and Mrk 509.

Mrk 79 is an interesting target because while the EW of component 1 is variable, the continuum does not change. This lends itself to a case of changing the total column, most likely due to bulk motion. We can calculate the transverse velocity by using the measured broad line diameter from Peterson et al. (1998) of 36 light days and a time interval between observations (Δt) of 83.7 days the absorber would be moving at a transverse velocity $\geq 126,000$ km s⁻¹. Given the average radial velocity of the absorber $v_r \approx 300$ km s⁻¹, the estimate for the transverse velocity is inordinately high. We will tackle further explanations in the next section.

In the case of Mrk 817, if we assume that the appearance of the new absorption components (2 and 3) are due to transverse motion of material into the line of sight, we can follow the methods used by Gabel et al. (2005) for NGC 3783. Assuming the O VI doublet is not saturated we can use the covering factor in the line of sight for O VI at the conclusion of

the variability event with the equation:

$$C_f = \frac{I_1^2 - 2I_1 + 1}{I_2 - 2I_1 + 1} \quad (2)$$

(Crenshaw et al. 2003), where I_1 is the intensity at the core of the stronger oscillator strength line and I_2 is for the weaker line. This number can be skewed an by additional flux from the Narrow Emission Line Region (NELR) (Kraemer et al. 2002, Arav et al. 2002, Crenshaw et al. 2003), but for Mrk 817 the narrow emission lines are not prominent, and we find $C_f = 0.70$. If we compare this to the line-of-sight covering factor of 0.51 and 0.33 for the blue and red lines respectively we verify that the lines are not saturated due to the fact that as lines approach saturation in a doublet, the line-of-sight covering factor approaches the doublet covering factor. The transverse size of the absorbing cloud is $d=d_{BLR} \times \sqrt{C_f}$ (Crenshaw et al. 2003). For Mrk 817, the BLR is 31 light-days across (Peterson et al. 1998). The absorption appeared over ~ 310 days, which gives a lower limit to the transverse velocity of $\sim 25,100 \text{ km s}^{-1}$. This is exceptionally large compared to the radial velocity of 3700 and 3430 km s^{-1} for the two new components. Thus, either the components were buried in the noise in the earlier observations or we are witnessing their appearance due to ionization changes.

Mrk 509 was shown in Peterson et al. (1998) to have a BLR size of 159 light days. If we assume that subcomponents 3 and 6 are saturated in $\text{Ly}\beta$, then we can calculate the change in covering factor (C_f) from the residual intensities in the cores ($C_f = 1 - I_r$). In the case of subcomponent 6, we measured the core and found average covering factors $C_f=0.78$ and 0.96 for observations 1 and 3 ($\Delta t=307.3$ days). For subcomponent 3, we find covering factors $C_f=0.93$ and 0.77 for observations 2 and 3 ($\Delta t=304.0$ days). Subcomponent 6 therefore, showed an increase in covering factor by 0.18 while subcomponent 3 showed a decrease by 0.16. Based on the changes in covering factors, from our previous equation we can find lower limits for transverse velocity for these of 65,600 km s^{-1} for subcomponent 6 and 125,200 km s^{-1} for subcomponent 3. This seems extremely high for a transverse velocity when compared to the radial velocities of $\sim 300 \text{ km s}^{-1}$. Therefore, the changes in the depths of these two subcomponents are almost certainly due to ionic column variation and not covering factor changes.

Thus, even in the most favorable cases, we find no evidence for EW changes due to bulk motion. Because there is no evidence that transverse velocities of UV absorbers can reach these inordinately high values (Crenshaw et al. 2003), the only viable alternative is ionic column changes due to changes in the ionizing continuum.

6.2. Ionization Changes

The three objects we have ruled out bulk motion for and the other six objects that showed signs of absorption variability all seem to be the result of changes in the ionizing flux. Mrk 279 and Mrk 290 showed an anticorrelation between ionization parameter (U) and O VI EW, while NGC 3783 showed anticorrelation in $\text{Ly}\beta$. For Mrk 279 and Mrk 290 this means that the ionization state is high, and NGC 3783 is indeterminate due to no detectable change in O VI. Mrk 817, component 1, is the only case where the EW for O VI is correlated with the flux, which means that U is relatively low. For NGC 4151 we see the D' component decrease with increasing flux, thus it is another high- U component. PG 0804+764 showed correlation between flux and EW for both the O VIIb line and $\text{Ly}\beta$. This object stands out because it is the only object in the survey that showed an unexplainable change in radial velocity.

Mrk 79 showed a change in EW and no change in flux. Because we only have three observations, we believe what we are seeing a change in ionization with a time delay. Our observations do not accurately sample the lightcurve and there must be a delay between the EW response and the continuum, due to low densities and/or large distances of the absorbers from the continuum source (Crenshaw et al. 2003).

The appearance of the absorption components 2 and 3 in Mrk 817 is most likely due to a change in ionization. The light curve shown at the bottom of Fig. 11, shows that in the last observation where the two components are visible, the flux level had decreased significantly. The appearance of these lines may therefore be due to a decrease in ionizing flux. We can also use the possible disappearing subcomponent in component 1 to place limitations on the absorption systems. As the continuum flux decreases the line weakens and vanishes/blends with the component at $\sim 1049.2 \text{ \AA}$, and could be the explanation of the EW variations we noted in §5. In order to place these constraints, we need CLOUDY modeling of the absorbers.

Mrk 279 presents a similar situation. In Figure 13 we have a range of ~ 58 days where the continuum flux drops and rises. The EW for the absorbers respond by decreasing. We could estimate a lower limit to the distance and density provided a model of the absorber and assuming the response is complete after 58 days. Ideally, we would need a monitoring campaign with several observations for an event such as this to fully explain the variations.

For the component Kraemer et al. (2002) labeled 3 in Mrk 509, we can assume that the ionizing flux increased and the column changed. We know from Kraemer et al. (2003) that the ionization parameter (U) for Mrk 509 in subcomponent 3 is 0.03. Given the change in

time, $\Delta t = 2.6 \times 10^7$ s, we can use the equation as seen in Krolik & Kriss (1995):

$$t_{ion} = \frac{h\nu}{F_{ion} \langle \sigma_{ion} \rangle}, \quad (3)$$

where ν is the transition frequency, F_{ion} is the ionizing flux at the cloud front and $\langle \sigma_{ion} \rangle$ is the ionization cross section (Osterbrock 1989). Using our known limit on the timescale, and a calculated value of $L_{ion} = 2.1 \times 10^{44}$ ergs s⁻¹, we can get a limit on the distance from the source to the cloud from $F_{ion} = L_{ion} / 4\pi d^2$. That gives us the lower limit to the distance of 14 pc.

Finally, we can estimate the density of the absorbing cloud assuming a change in ionization, from the ionization parameter:

$$U = \frac{\int \frac{L_\nu d\nu}{h\nu}}{4\pi c r^2 n_e} \quad (4)$$

For our subcomponent 3 we find $n_e \leq 1.38 \times 10^3$ cm⁻³.

6.3. NALs and BALs

From both the Paper I survey and the Laor & Brandt surveys, one object, PG 1411+442, appeared in both surveys with BAL and NAL signatures. The NALs appear superimposed on the BAL in both members of the O VI doublet, as seen in Paper I. This evidence tied with the Laor & Brandt and our relationship from section §4, shows that both BALs and NALs are related and follow the same trends and that they both may exist simultaneously in an object.

Also from our previous survey, WPVS 007 was omitted from the search for NALs due to the discovery of a newly appearing BAL by Leighly et al. (2007, in prep). We have reexamined this object and found that the NALs seen by Crenshaw et al. (1999) are still visible in the *FUSE* spectrum. The NALs for O VI and Ly β are buried in the BAL and have a velocity of -399 ± 10 km s⁻¹ seen in Figure 23. This matches the velocity Crenshaw et al. (1999) found of -390 km s⁻¹.

We can evaluate the configuration of the NAL and the appearing BAL in WPVS 007. The time difference between the *FUSE* spectrum and the last FOS spectrum is 2655 days. If we use the relationship from Vestergaard & Peterson (2006):

$$R \propto L_\nu(\lambda 5100)^{0.50 \pm 0.06}, \quad (5)$$

with a BLR size that has been estimated from reverberation mapping, we find that the BLR size for WPVS 007 is ~ 23 light days across. This gives a lower limit on the transverse velocity

of the BAL of 2565 km s^{-1} . The NAL however is still apparent in the O VI doublet and Lyman β lines. This leaves us with two situations. Either the NAL is interior to the BAL and is still receiving sufficient ionizing flux to maintain the absorption, or the NAL is exterior to the BAL and is no longer receiving ionizing flux due to the BAL absorption. If the latter is true, then the recombination timescale is larger than the 2655 days between observations, which could be used to estimate a density and distance provided photoionization modeling.

7. Conclusions

Our goal was to explore the Dunn et al. (2007) *FUSE* survey in depth for correlations and variability. We sought to characterize the intrinsic absorption seen in nearly 50% of all nearby active galaxies in order to help characterize the outflow from the nuclear engine.

As shown by Laor & Brandt (2002), there is a relation between the maximum outflow velocity and the luminosity. Their survey contained moderate redshift objects and BAL quasars, while our survey was for smaller redshifts and luminosities. However, as shown previously, our relation between v_{max} and L is consistent with theirs. In both our surveys there is a distinct upper limit on the maximum velocity dependent upon the luminosity of the object. This leads us to believe that both classical narrow intrinsic absorption lines and broad absorption lines are governed by the same relationship, thus they may be related, in the sense that they may share a common driving mechanism. Due to their simultaneous presence in WPVS 007 and PG 1411+442 however, we feel that the nature of their origins may be different.

Laor & Brandt (2002) also found for higher redshift galaxies that EW & luminosity are correlated for C IV. We examined correlations between the observed lines and the AGN properties. We found no link between the EW and the luminosity. Because EW increases with column density of the particular ion in question, it would seem that an increase in flux would increase the O VI EW in cases where the ionization parameter is low and vice versa for a highly ionized cloud, at least until the line reaches heavy saturation. We do not see this trend for either O VI or Ly β . This is most likely due to the heavy saturation in O VI and even Ly β in many cases while C IV and N V do not saturate as easily.

It has been seen in the past that some objects show bulk transverse motion along with the more easily detectable radial motion (Crenshaw et al. 2003). Of the 35 objects available we have 22 with more than one observation. Two of these objects have only one usable observation, leaving 20 total useful data sets. In the survey we find 8 that show change. The frequency of variability events seems to be low, in the *FUSE* data. With 22 available objects,

only 8 show variability. This could mean the events are rare, that only weak absorption is subject to this change and/or the sample is biased by small number statistics, or the O VI saturation makes detecting variability difficult.

None of our objects with EW changes can be explained with transverse bulk motion. We have 7 that can be explained with ionization changes. In the case of Mrk 509 with modeling of the subcomponents, we can find a distance and density (n_H) of the third subcomponent of 0.3 pc and $3.8 \times 10^8 \text{ cm}^{-3}$, respectively. Also, we find one object that shows evidence for radial velocity changes (PG 0804+761); we currently have no explanation for this.

We find in Mrk 817 that the absorption appears in relatively weak lines, and furthermore even the changes in the absorption features for Mrk 509 are in relatively weak lines. This is the case for most transversely moving clouds seen in the past. With the low signal-to-noise *FUSE* data it may be that these weak lines are swamped by the surrounding noise and only strong absorption features are noticeable, or it may be that bulk transverse motion is not a common event. Given that these changes are in weak absorbers, it suggests that strong absorbers appear more static in the far UV than weak absorbers due to saturation and blending in many of the lines.

This research has made use of the NASA/IPAC Extragalactic Database (NED) which is operated by the Jet Propulsion Laboratory, California Institute of Technology, under contract with the National Aeronautics and Space Administration. This research has also made use of NASA's Astrophysics Data System Abstract Service. We acknowledge support of this research under NASA grants NNG05GC55G, NNG06G185G and NAG5-13109.

REFERENCES

- Anderson, K. S., & Kraft, R. P. 1969, *ApJ*, 158, 859
- Arav, N., Li, Z.-Y. & Begelman, M. C. 1994, *ApJ*, 432, 62
- Arav, N., Korista, K. T. & de Kool, M. 2002, *ApJ*, 566, 699
- Begelman, M. C., McKee, C. F., & Shields, G. A. 1983, *ApJ*, 271, 70
- Blandford R. D. & Payne D. G. 1982, *MNRAS*, 199, 883
- Boroson T. A. & Green R. F. 1992, *ApJS*, 80, 109
- Botte, V., Ciroti, S., Rafanelli, P. & Di Mille, F. 2004, *AJ*, 127, 3168
- Crenshaw, D. M., Kraemer, S. B., Boggess, A., Maran, S. P., Mushotzky, R. F., & Wu, C.-C. 1999, *ApJ*, 516, 750
- Crenshaw, D. M., Kraemer, S.B., & George, I.M. 2003, *ARA&A*, 41, 117
- Cromwell, R., & Weymann, R. 1970, *ApJ*, 159, 147
- Dixon, W. V. D., Kruk, J. & Murphy, E. 2002, *The CalFUSE Pipeline Reference Guide*
- deKool, M. & Begelman, M. C. 1995, *ApJ*, 455, 448
- Dunn, J. P., Jackson, B., Deo, R. P., Farrington, C., Das, V., & Crenshaw, D. M. 2006, *PASP*, 118, 572
- Dunn, J. P., Crenshaw, D. M., Kraemer, S.B., & Gabel, J. R. 2007, *AJ*, 134, 1061 (Paper I)
- Feldman, P. D., Sahnou, D. J., Kruk, J. W., Murphy, E. M. & Moos, H. W. 2001, *JGR*, 106.8119
- Foltz, C. B., Chaffee, F. H., Hewett, P. C., Weymann, R. J., & Morris, S. L. 1990, *AAS*, 22, 806
- Gabel, J. et al. 2005, *ApJ*, 631, 741
- Gabel, J. et al. 2003, *ApJ*, 595, 120
- Ganguly, R., Masiero, J., Charlton, J. C., Sembach, K. R. 2003, *ApJ*, 598, 922
- Ganguly, R., Brotherton, M. S., Cales, S., Scoggins, B., Shang, Z., & Vestergaard, M. 2007, 665, 990
- Ganguly, R. & Brotherton, M. S. 2008, *ApJ*, 672, 102
- Gillmon, K., Shull, J. M., Tumlinson, J. & Danforth, C. 2006, *ApJ*, 636, 891
- Grupe, D. & Mathur, S. 2004, *ApJ*, 606, 41
- Khachikian & Weedman 1974, *ApJ*, 192, 581

- Kaspi et al. 2000, ApJ, 533, 631
- Kraemer, S. B., Turner, T. J., Crenshaw, D. M. & George, I. M. 1999, ApJ, 519, 69
- Kraemer, S. B., Crenshaw, D. M., & Gabel, J. R. 2001, ApJ, 557, 30
- Kraemer, S. B., Crenshaw, D. M., Yaqoob, T., McKernan, B., Gabel, J. R., George, I. M., Turner, T. J. & Dunn, J. P. 2002, ApJ, 582, 125
- Kraemer et al. 2003, ApJ, 582, 125
- Kraemer et al. 2005, ApJ, 633, 693
- Kraemer, S. B., Crenshaw, D. M., Gabel, J. R., Kriss, G. A., Netzer, H., Peterson, B. M., George, I. M., Gull, T. R., Hutchings, J. B., Mushotzky, R. F. & Turner, T. J. 2006, ApJS, 167, 161
- Kriss, G. A. 2002, ASPC, 255, 69
- Krolik, J. H. & Kriss, G. A. 1995 ApJ, 447, 512
- Laor, A. & Brandt, W. N. 2002, ApJ, 569, 641
- Mason et al. 1995, MNRAS, 274, 1194
- Maran, S. P., Crenshaw, D. M., Mushotzky, R. F., Reichert, G. A., Carpenter, K. G., Smith, A. M., Hutchings, J. B., Weymann, R. J. 1996, ApJ, 465, 733
- Marziani, P., Sulentic, J. W., Zamanov, R., Calvani, M., Dultzin-Hacyan, D., Bachev, R. & Zwitter, T. 2003 ApJS, 145, 199
- McLure, R. J. & Dunlop, J. S. 2004, MNRAS, 352, 1390
- Morton, D. C. 1991, ApJS, 77, 119
- Osterbrock, D. E. 1989, Astrophysics of gaseous nebulae and active galactic nuclei (Research supported by the University of California, John Simon Guggenheim Memorial Foundation, University of Minnesota, et al. Mill Valley, CA, University Science Books, 1989, 422 p.)
- Penton, S. V., Stocke, J. T. & Shull, J. M. 2002 ApJ, 565, 720
- Peterson, B. M., Wanders, I., Bertram, R., Hunley, J. F., Pogge, R. W., & Wagner, R. M. 1998, ApJ, 501, 82
- Peterson et al. 2004, ApJ, 613, 682
- Sahnou et al. 2000, ApJ, 538, 7
- Sahnou, D. 2002, The *FUSE* Instrument and Data Handbook
- Turnshek, D. A., Grillmair, C. J., Foltz, C. B. & Weymann, R. J. 1988, ApJ, 325, 651

Vestergaard, M. & Peterson B. M. 2006, ApJ, 641, 689

Weymann, R. J., Carswell, R. F., & Smith, M. G. 1981, ARA & A, 19, 41

Weymann, R. J., Morris, S. L., Gray, M. E., Hutchings, J. B. 1997, ApJ, 483, 717

Xu, D. W., Komossa, Stefanie, Wei, J. Y., Qian, Y. & Zheng, X. Z. 2003, ApJ, 590, 73

Fig. 1.— New spectra taken at CTIO, plotted in the observed frame.

Fig. 2.— The relation between luminosity and velocity using only data from *FUSE*.

Fig. 3.— Extended plot of luminosity and velocity using data measured by Laor & Brandt (2002). Crosses are data from our *FUSE* observations and asterisks are from the Laor & Brandt (2002) survey.

Fig. 4.— Relationship between Eddington Ratio and maximum outflow velocity. Crosses are objects with reverberation mapping.

Fig. 5.— EW vs. specific luminosity for our sample. The top plot is for O VI λ 1032, the middle is for O VI λ 1037 and the bottom plot is for Ly β . Plus symbols are components labeled 1 from Paper I and asterisks any component other than the first.

Fig. 6.— FWHM vs. specific luminosity. The top plot is for O VI λ 1032, the middle is for O VI λ 1037 and the bottom plot is for Ly β .

Fig. 7.— The available spectra for Mrk 79 plotted in order of increasing time from bottom to top. The upper spectra are offset by: 6.0×10^{-14} & 1.2×10^{-13} ergs s⁻¹ cm⁻² Å⁻¹. Component 1 (as identified by Paper I) is labeled by a dashed line and component 2 by a dotted and dashed line in each of the three lines (Ly β , O VIb and O VIr in order of increasing wavelength).

Fig. 8.— This plot shows the relation for each of the three lines between EW, average velocity & flux over time. Top to bottom the lines are plotted in order of decreasing wavelength. The dashed line represents the average value line of the data, which is mostly to guide the eye. The continuum seems to increase slightly while Ly β and O VI 1038 seem to vary.

Fig. 9.— Plotted in chronological order from bottom to top. The earlier spectra for NGC 4151 show the flattening of the region between 1029 and 1032 Å by an additional absorption component. The offsets for these data are: 4.0×10^{-13} , 8.0×10^{-13} & 1.2×10^{-12} ergs s⁻¹ cm⁻² Å⁻¹.

Fig. 10.— These spectra show the changes seen in Mrk 817. We see variability in the O VIb line, and find absorption appearing between 1051 and 1052 Å and 1056 and 1057 Å (components 2 and 3). There is one point we were able to measure the continuum for, but the lines were lost in the S/N. We have included the lightcurve point for completeness.

Fig. 11.— Mrk 817 relationships of EW, velocity and flux for component 1 over time. Both O VI lines show indications of decreasing EW with decreasing flux.

Fig. 12.— We present the spectral time series for Mrk 279 with offsets in flux of: 1.0, 2.5, 3.5, 5.0 & 6.0×10^{-13} ergs s⁻¹ cm⁻² Å⁻¹. This shows the variability seen in the lines.

Fig. 13.— Flux, EW and velocity against time for Mrk 279, similar to Figure 8. These quantities exhibit definite variability with time, and appears to be slightly anticorrelated with the flux. The last three points show signs of decrease in all three lines with the drop and rise of flux for those three observations, which hints at a lag in response time.

Fig. 14.— These are spectra of Mrk 290, which show the line trends with time (bottom to top). The offsets for these spectra are: 3.0×10^{-14} & 9.0×10^{-14} ergs s⁻¹ cm⁻² Å⁻¹.

Fig. 15.— We see in these plots (similar to Figure 8), that there is an decrease of EW with an increase in flux for all three lines. The trend for Lyman β is less convincing, however, due to the larger error bars.

Fig. 16.— We show the spectra for Mrk 509 and overplot the components 3 and 6 found by Kraemer et al. (2005), along with the dashed-dotted and dashed lines indicating our measured components 2 and 1 respectively. We have placed dotted lines to show the change in the slope of component 3 with respect to component 2. The offsets for these are: 2.5 & 5.0×10^{-13} ergs s⁻¹ cm⁻² Å⁻¹.

Fig. 17.— Mrk 509 relations for component 1, plotted similar to Figure 8.

Fig. 18.— Mrk 509 relations for component 2, plotted similar to Figure 8.

Fig. 19.— Spectra for PG 0804+761. The lines are marked with the dashed average velocity line, and the lines clearly appear to move. The dotted line labels a galactic Fe II line $\lambda 1044.2$ to show that the centroid for the ISM lines are not moving. Offsets for these are: 2.5, 5.0, 7.5×10^{-13} ergs s⁻¹ cm⁻² Å⁻¹.

Fig. 20.— PG 0804+761 relationships similar to Figure 8. We see definite correlations between velocity and EW with the flux levels with the exception of the Ly β EW which seems to be low in the second observation.

Fig. 21.— Spectra showing the time evolution of NGC 3783. The measured component is labeled with the dashed line. Offsets for these are: 1.5, 3.0, 4.5, 6.0, 7.5 & 9.0×10^{-13} ergs s⁻¹ cm⁻² Å⁻¹.

Fig. 22.— This shows the relation for NGC 3783 between EW, velocity and flux over time. Similar to Figure 8. We see definite variability in the EW over time for all three lines. There appears to be a possible correlation between the change in Ly β EW and continuum flux.

Fig. 23.— Spectrum for WPVS 007. The three absorption features are marked with dashed lines.

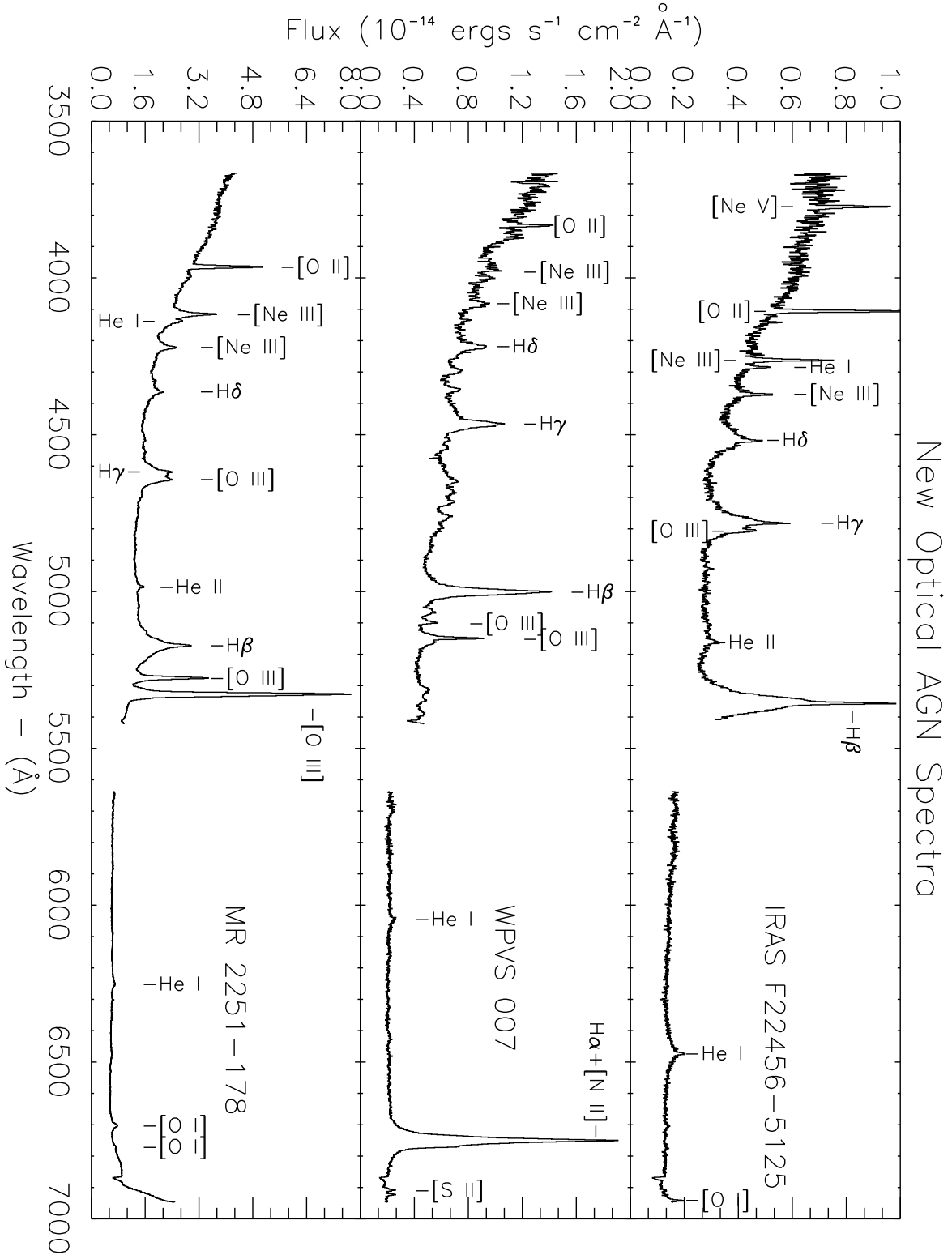


Fig. 1.

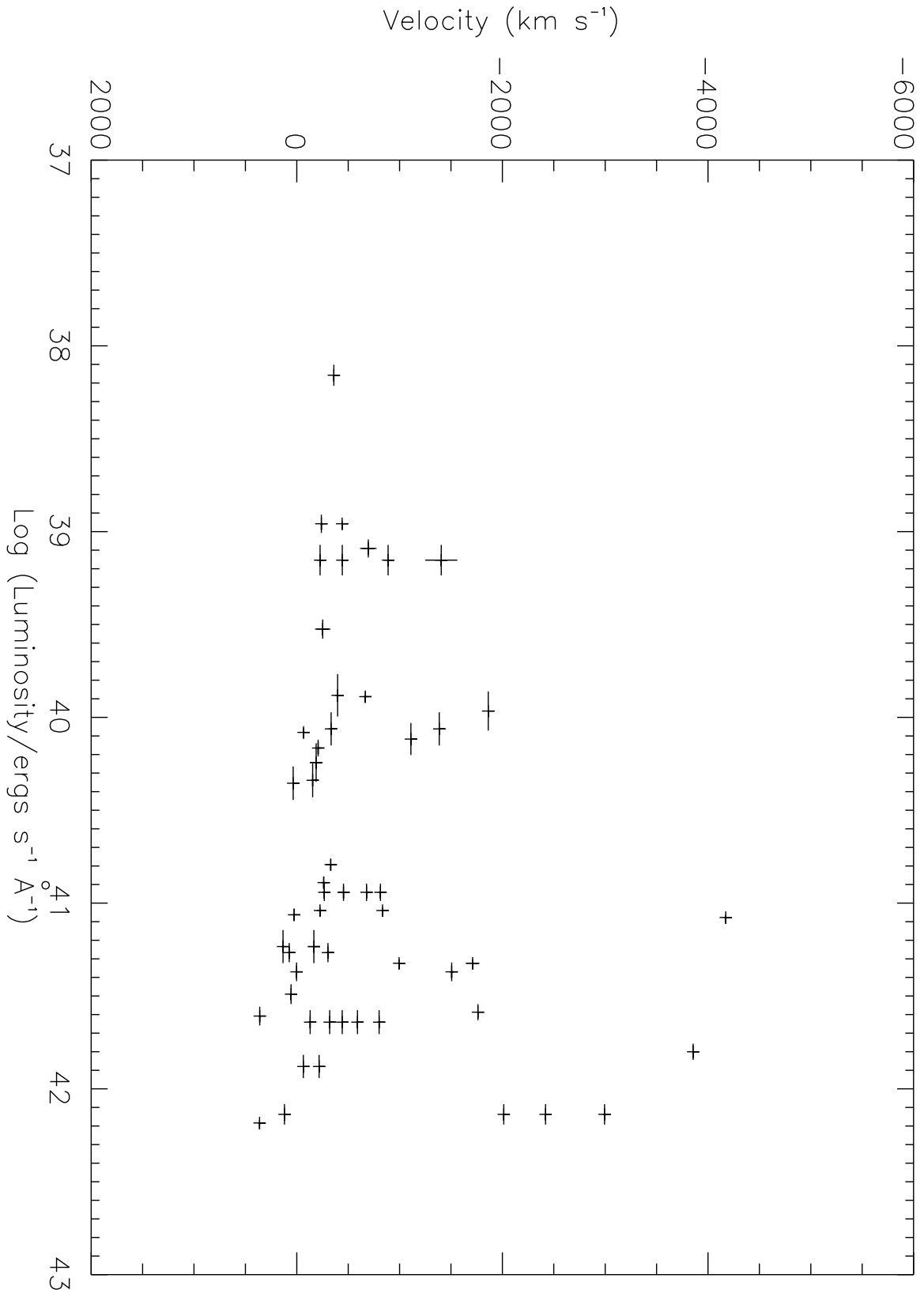


Fig. 2.

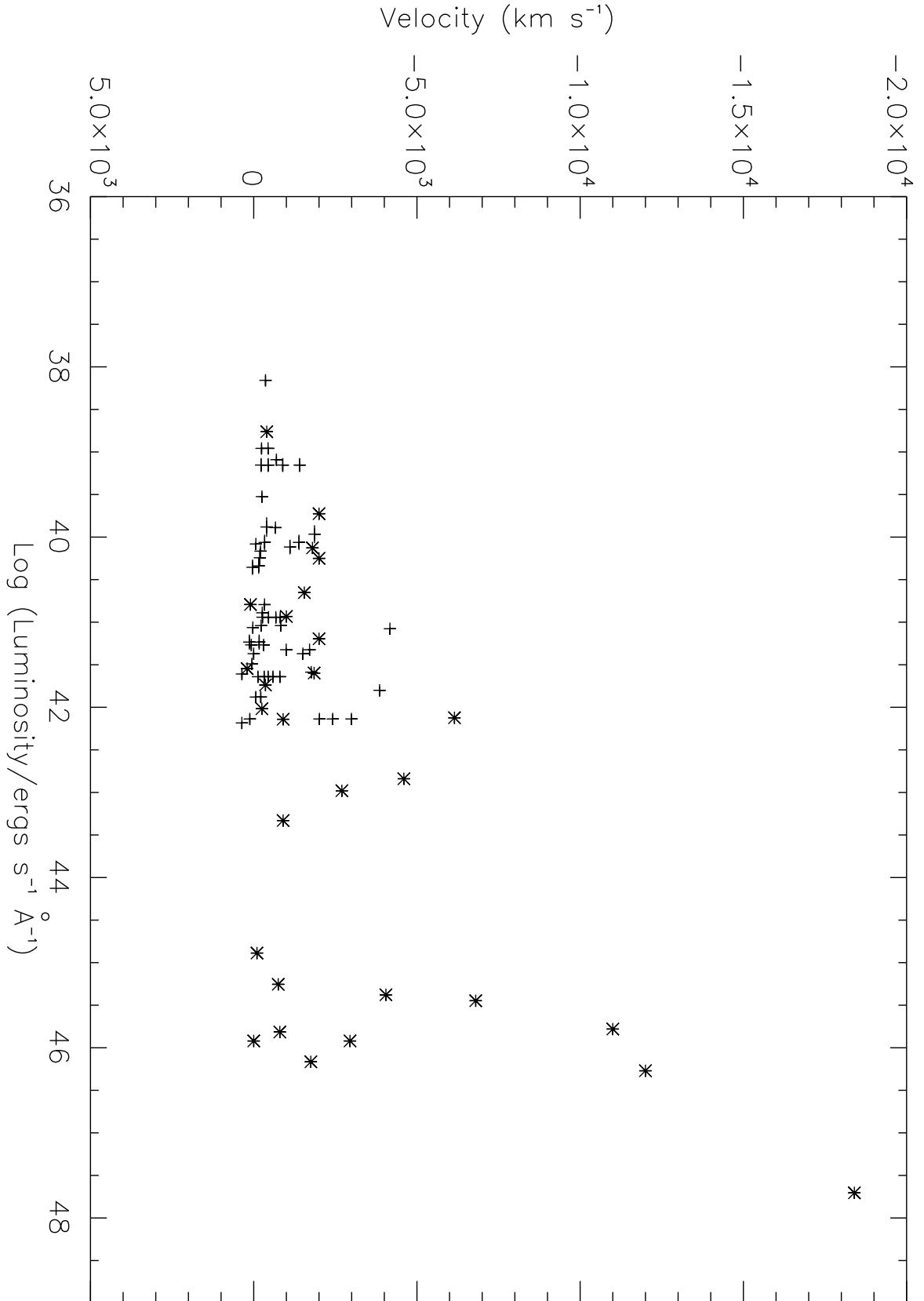


Fig. 3.

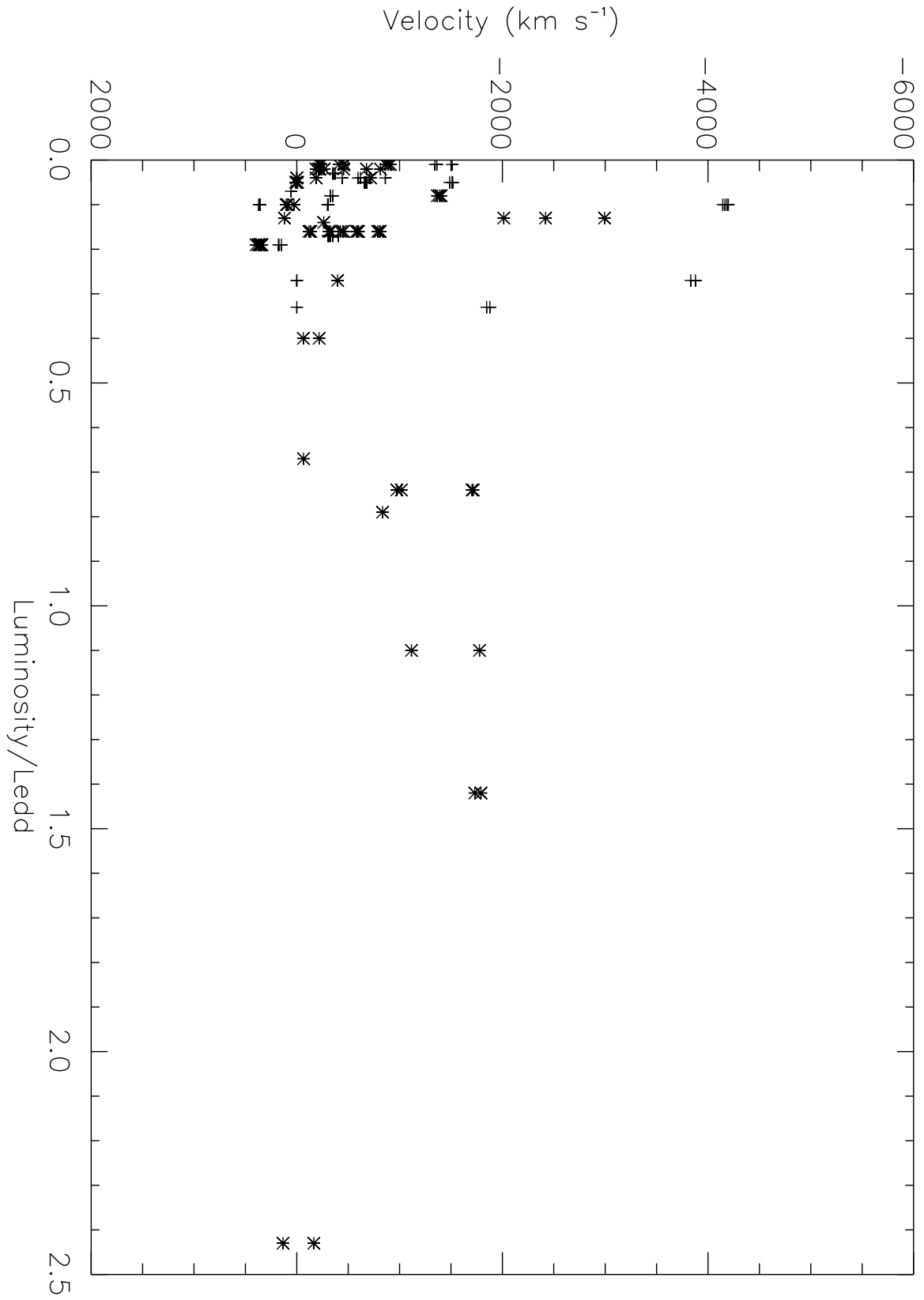


Fig. 4.

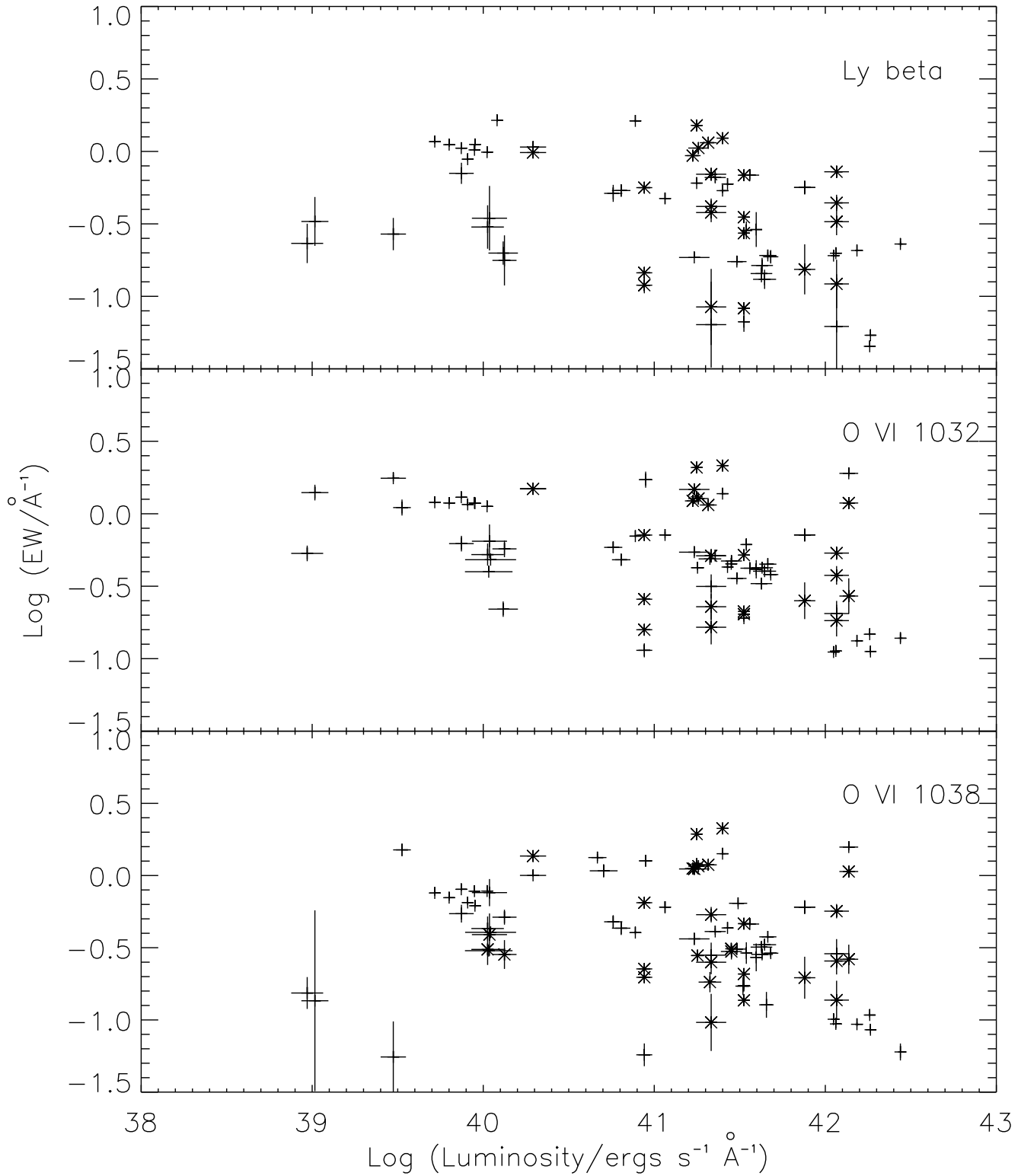


Fig. 5.

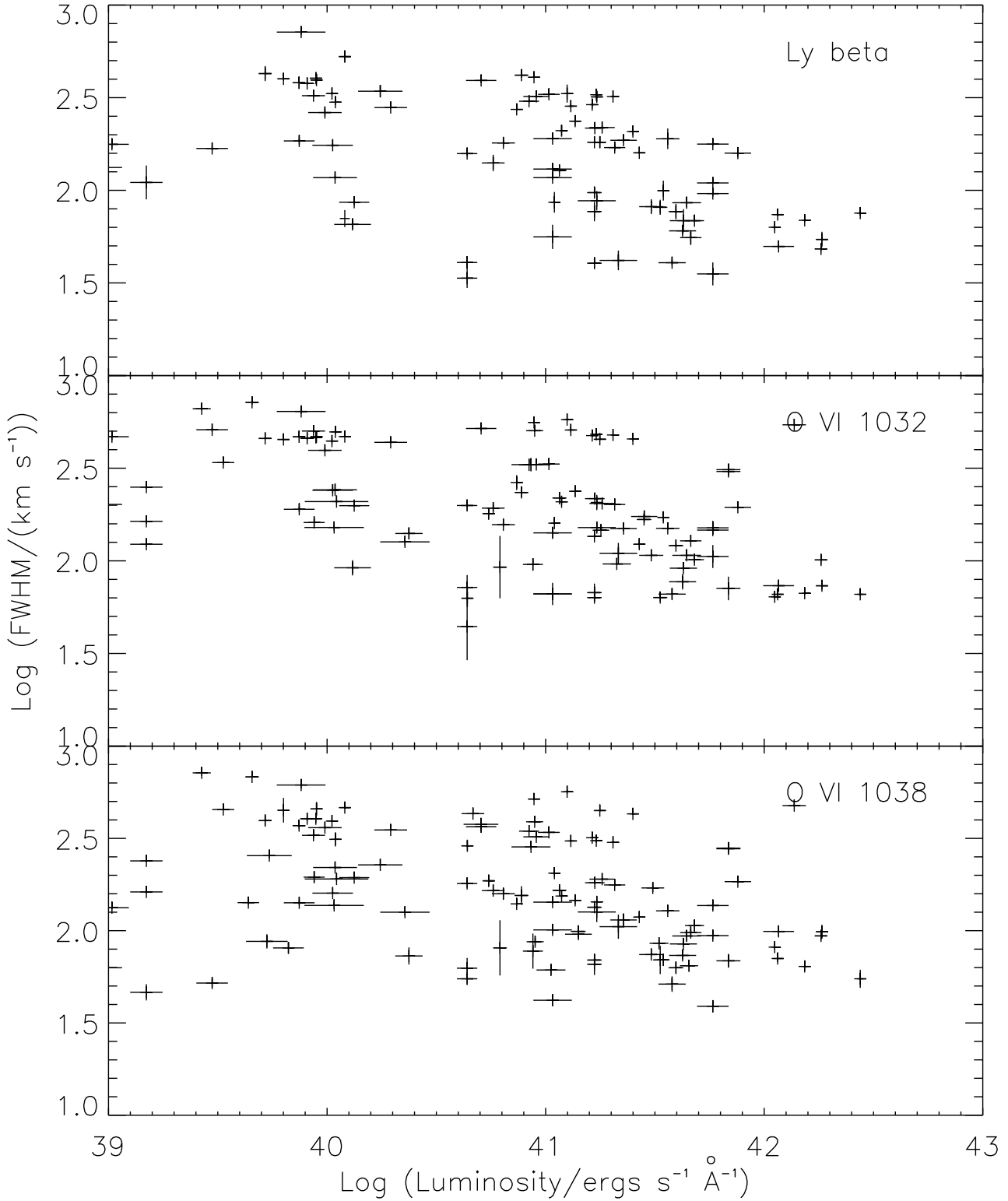


Fig. 6a.

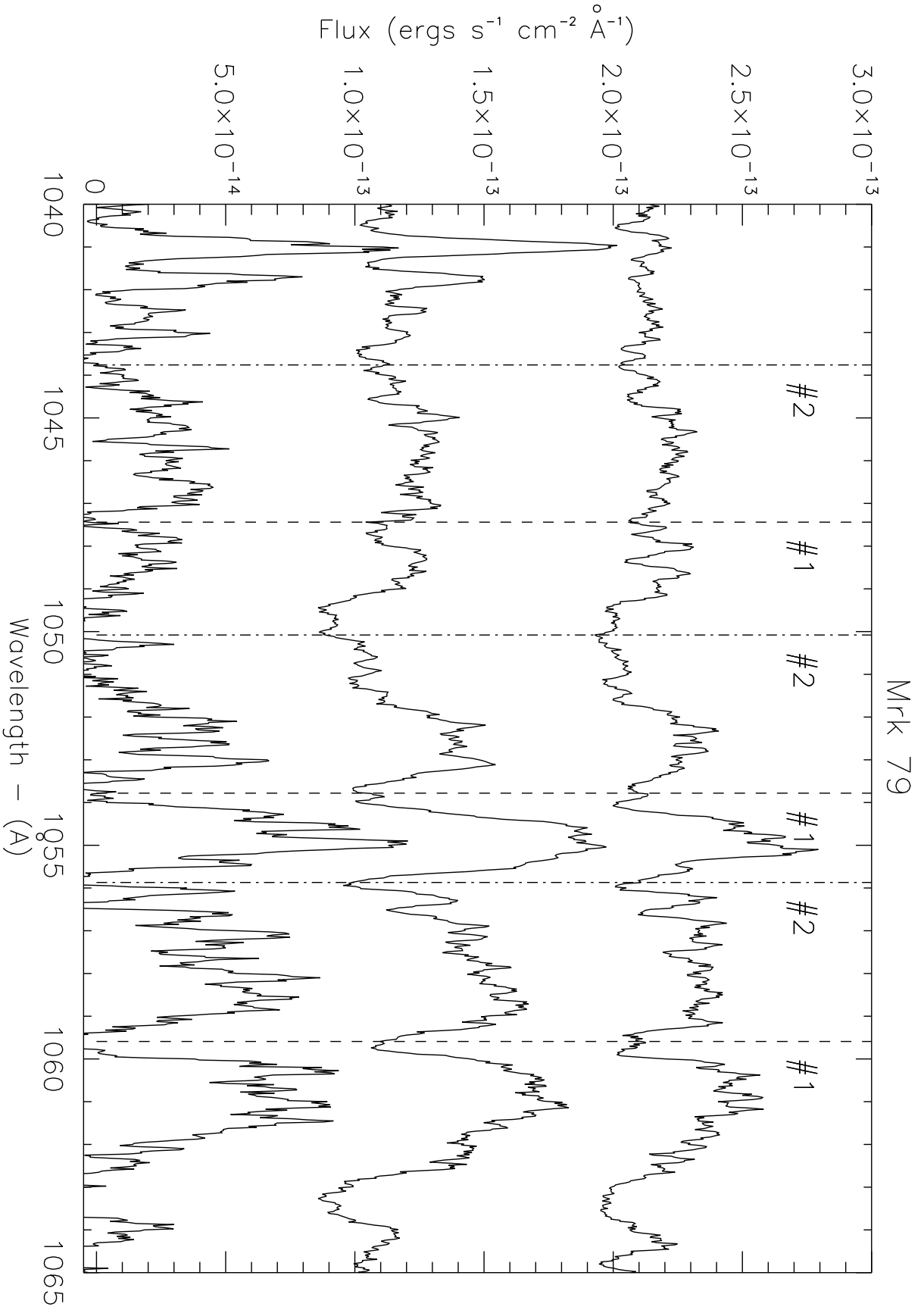


Fig. 7.

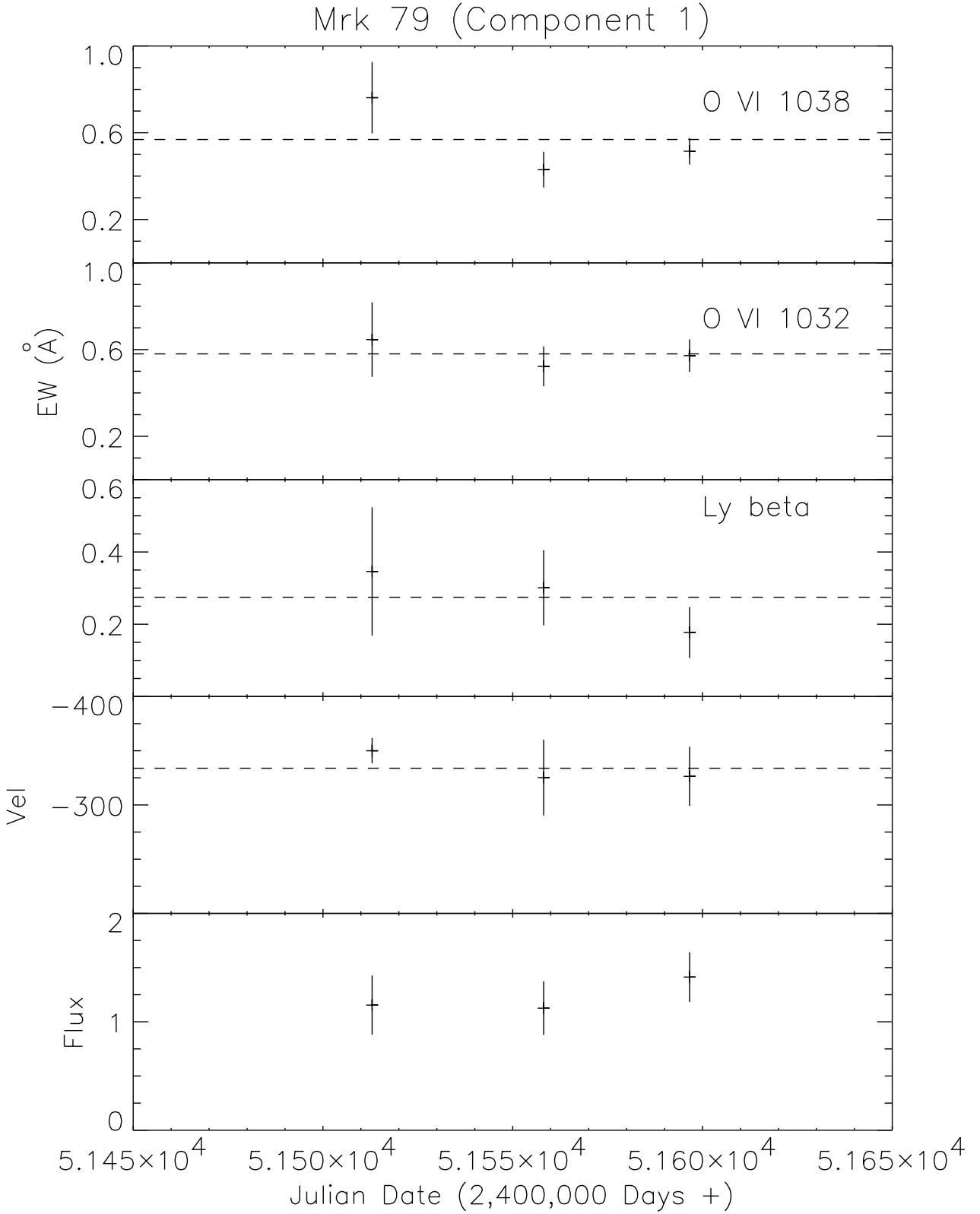


Fig. 8.

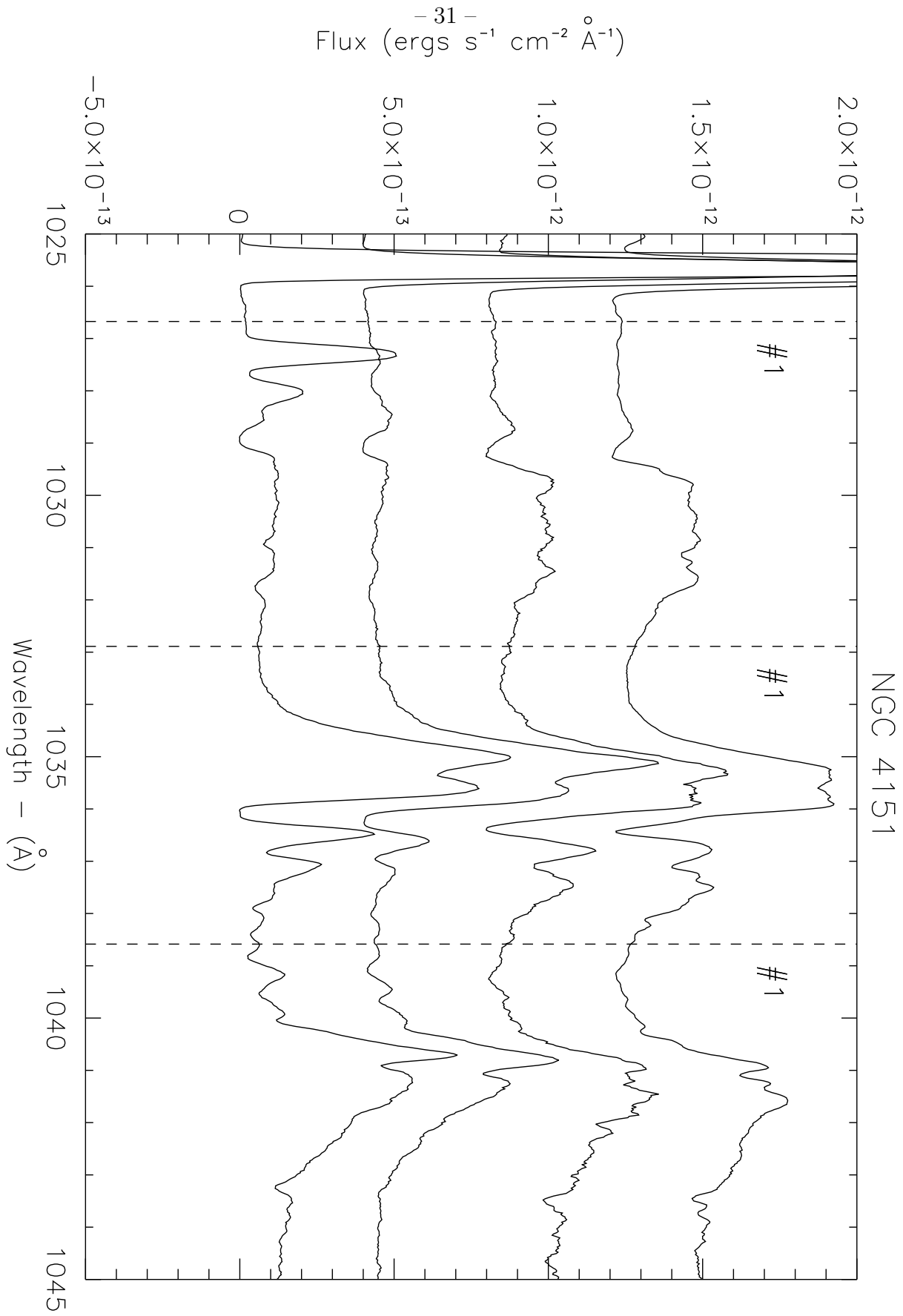


Fig. 9.

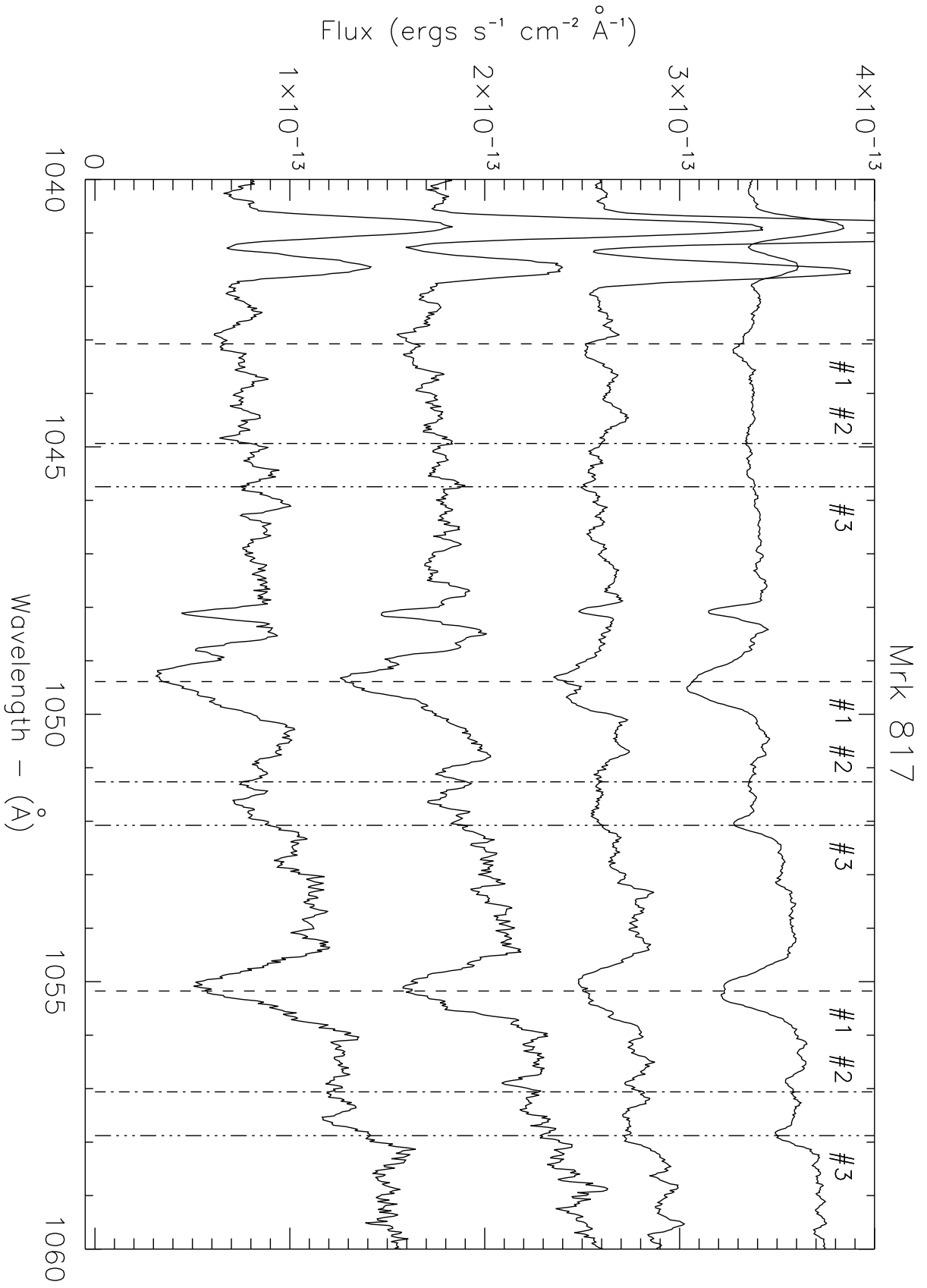


Fig. 10.

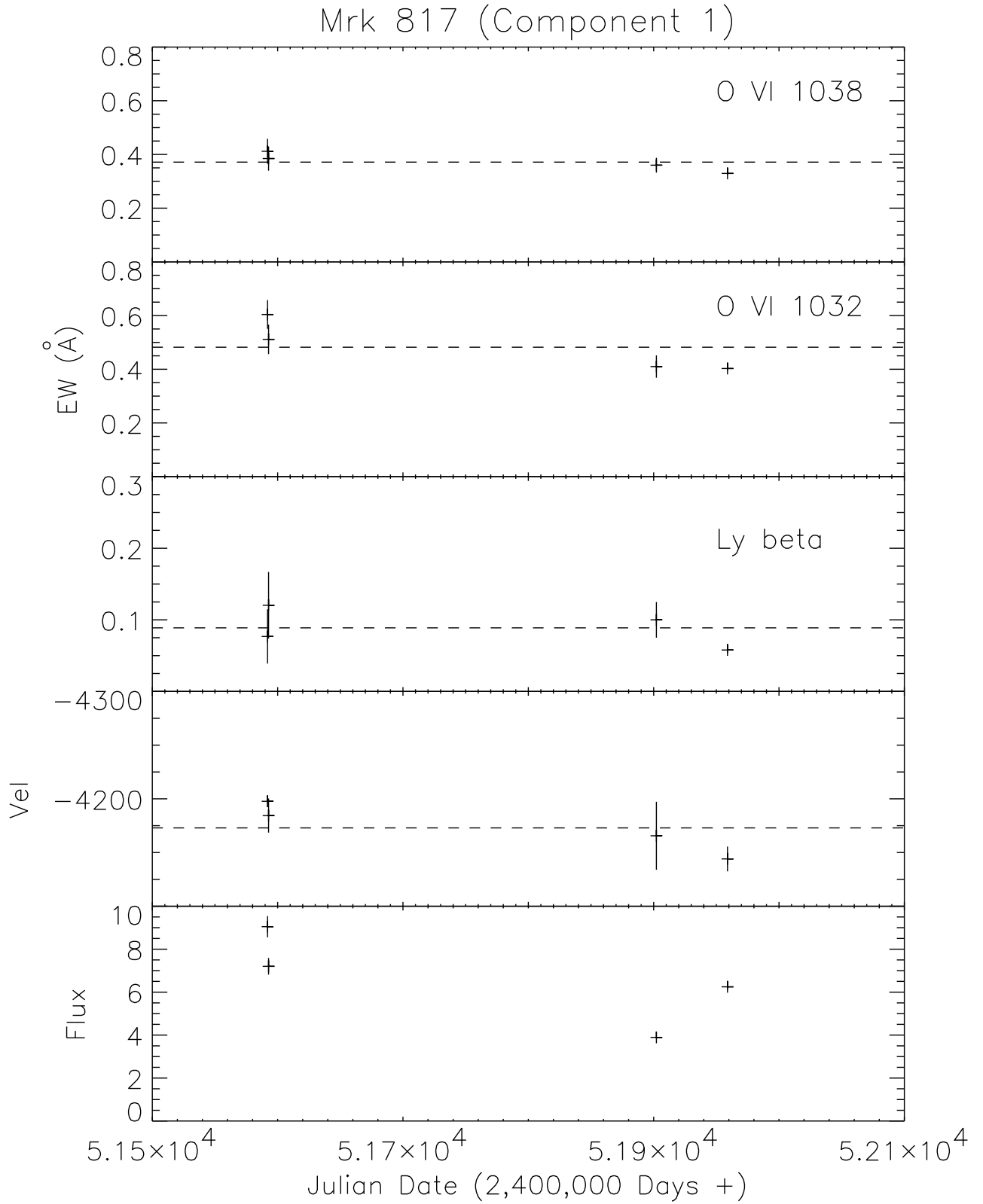


Fig. 11.

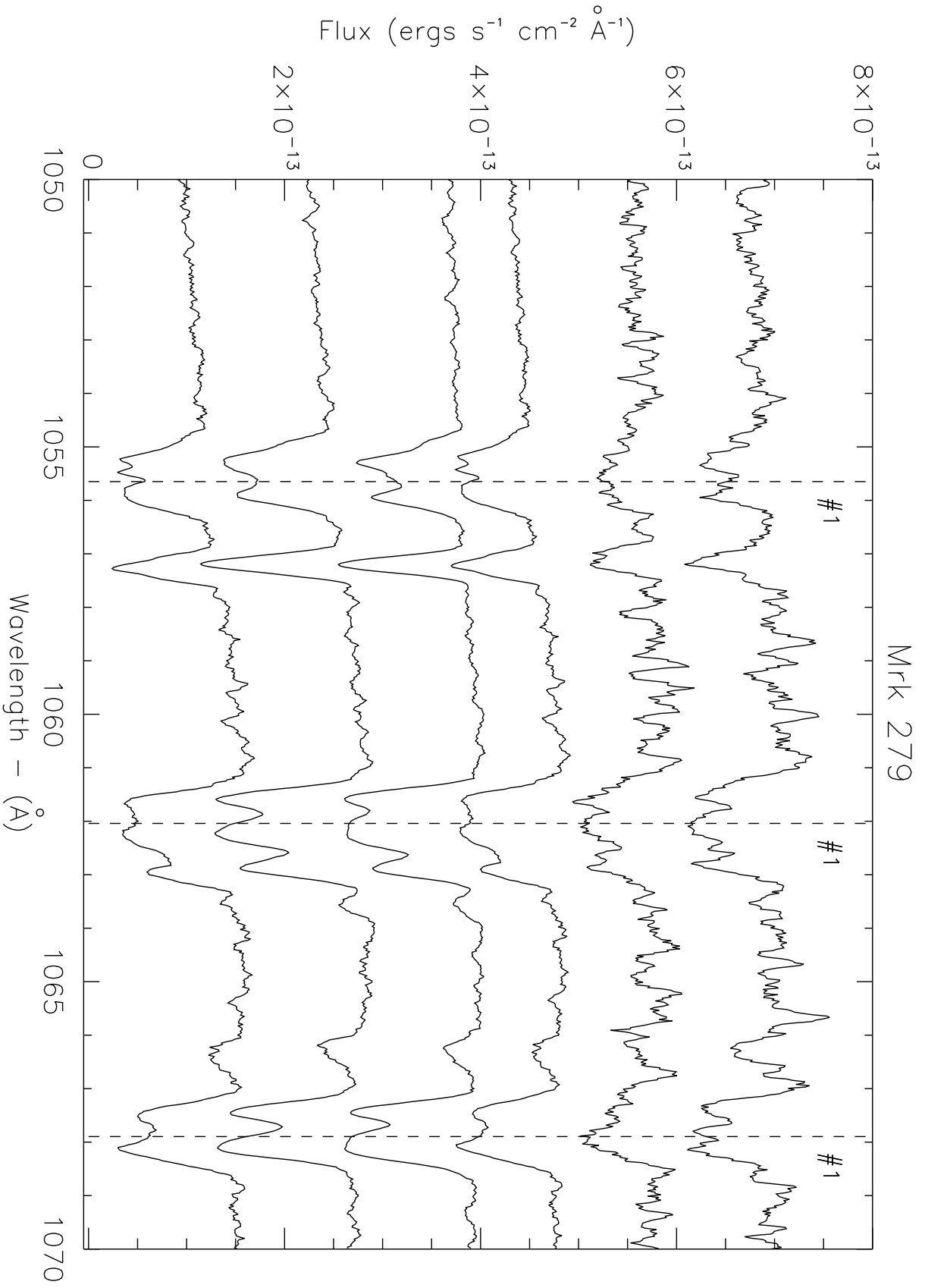


Fig. 12.

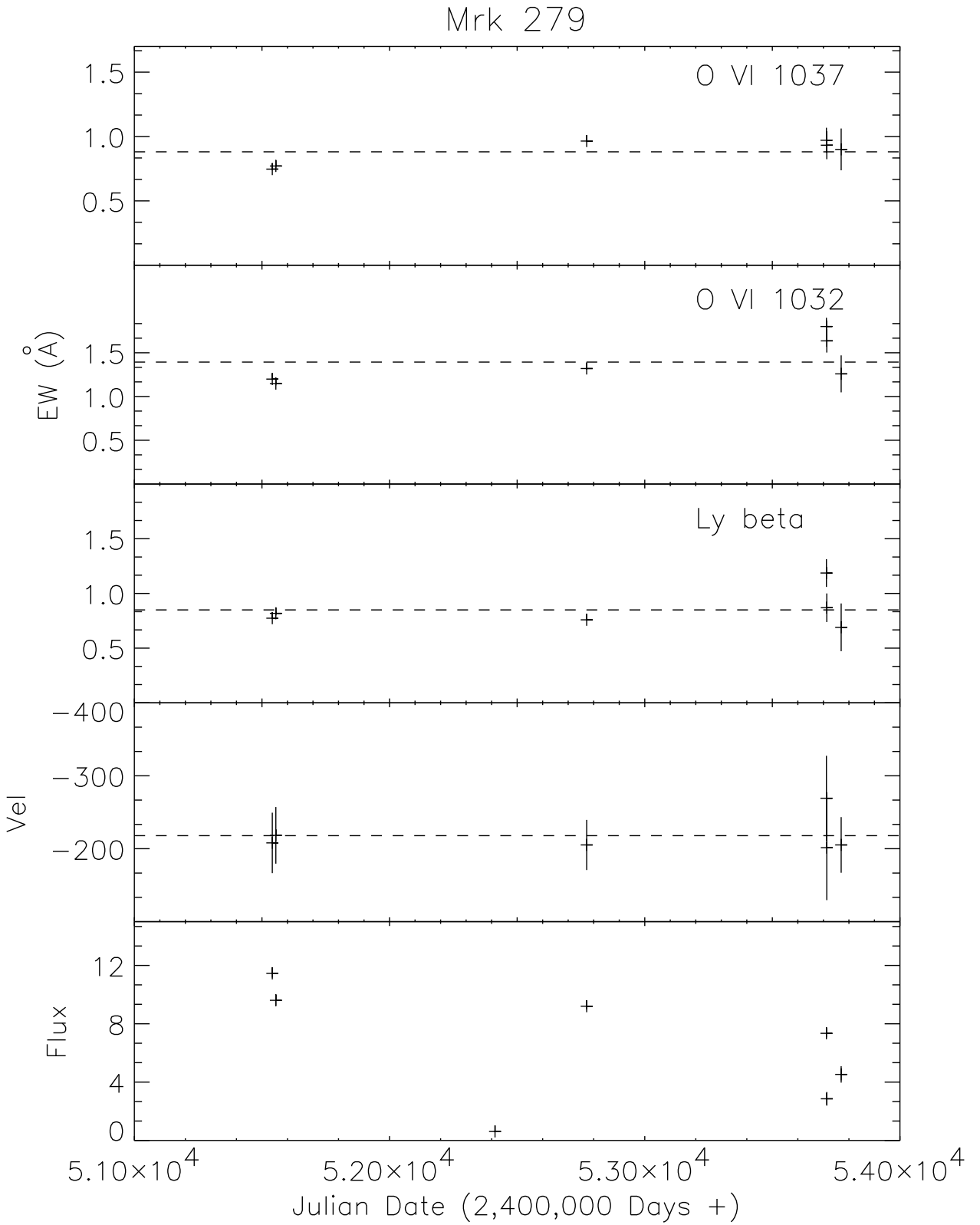


Fig. 13.

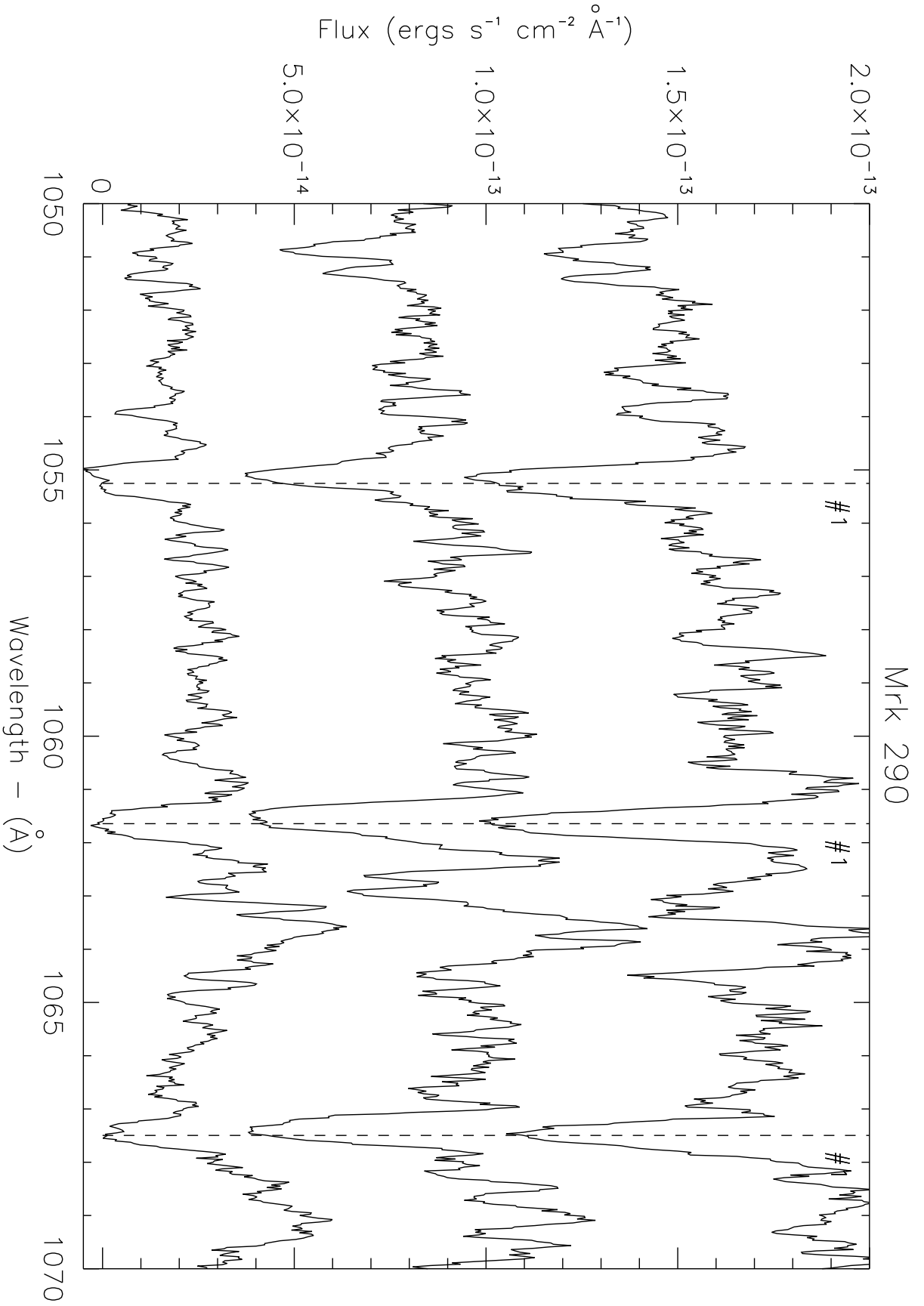


Fig. 14.

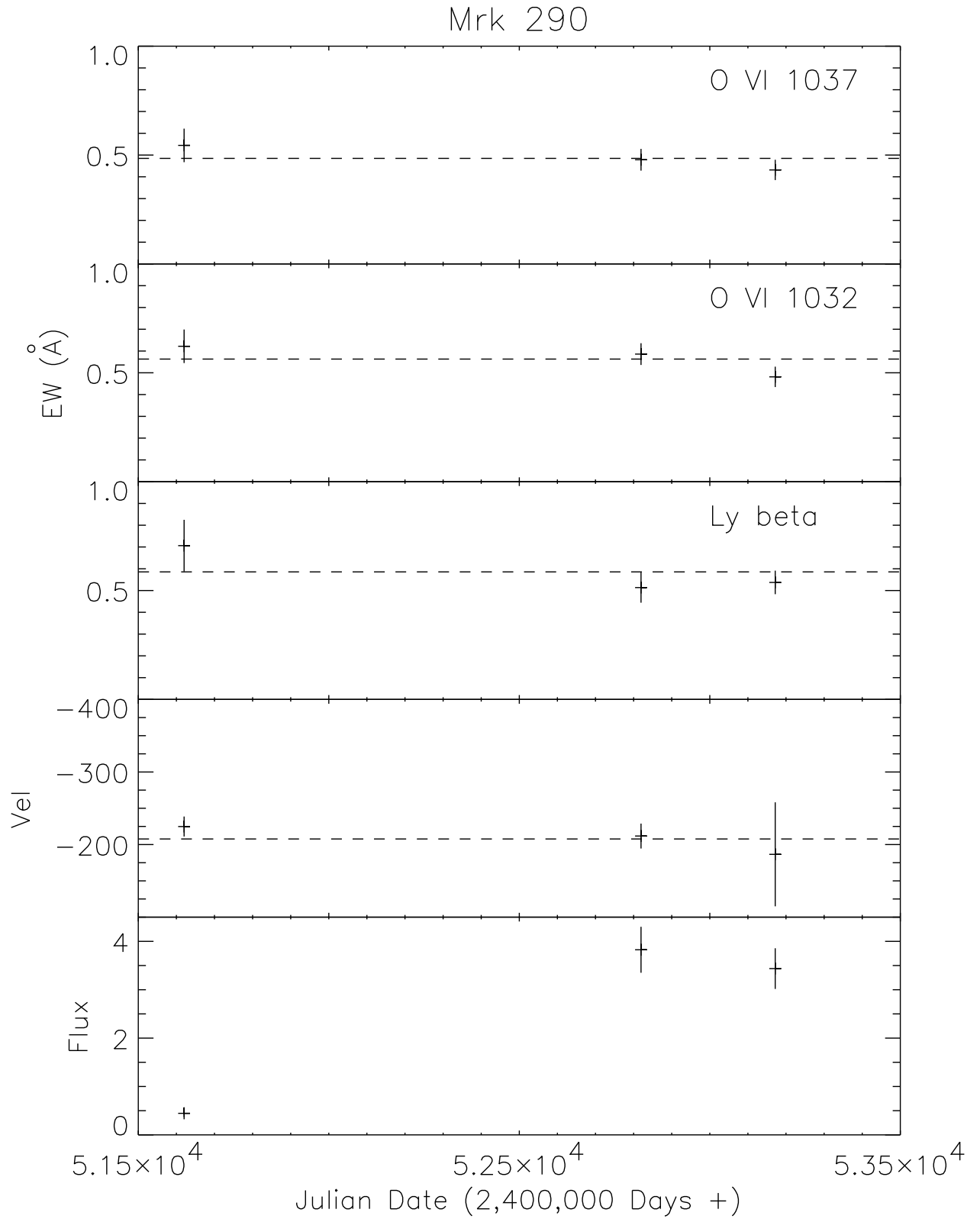


Fig. 15.

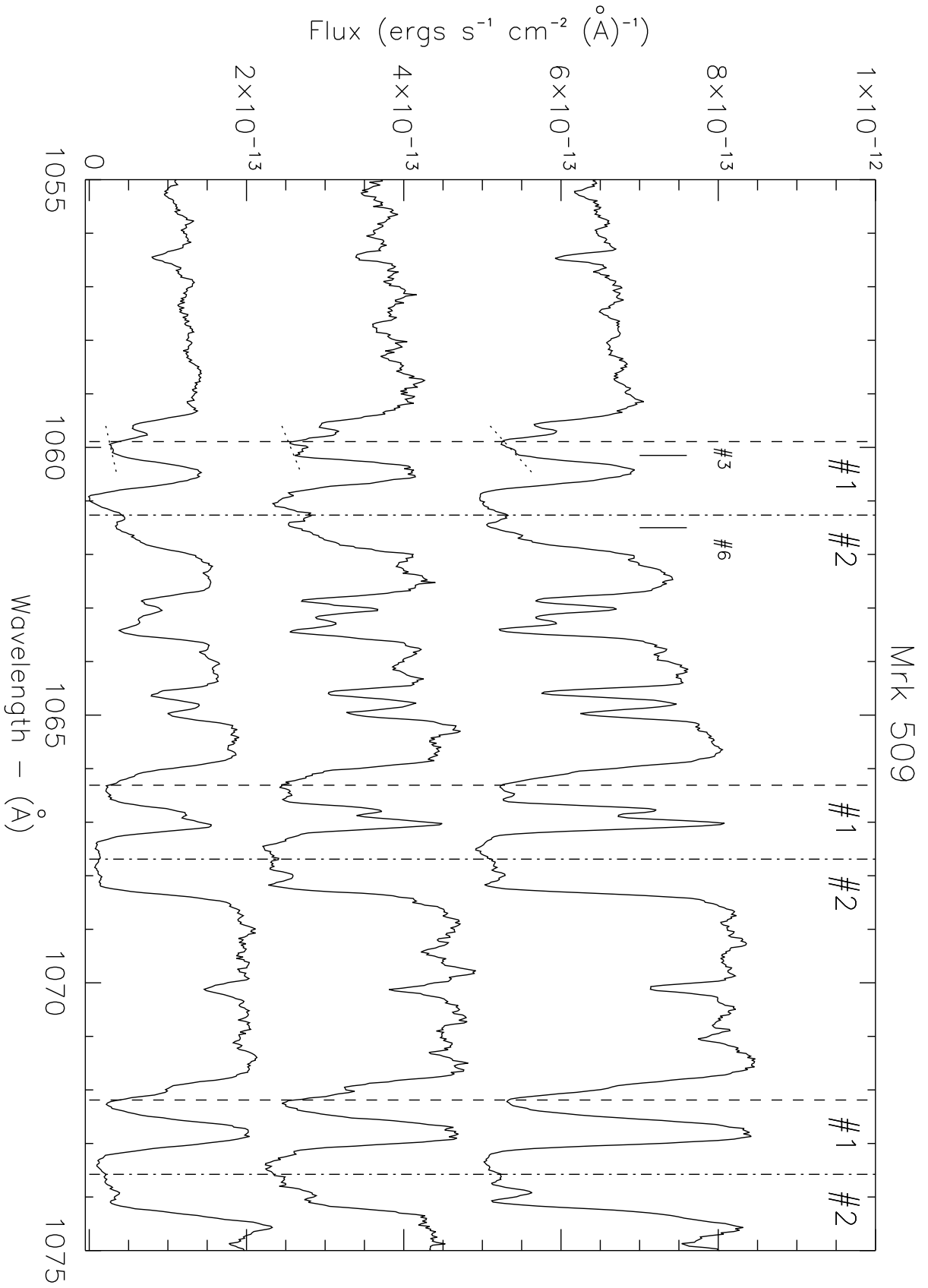


Fig. 16.

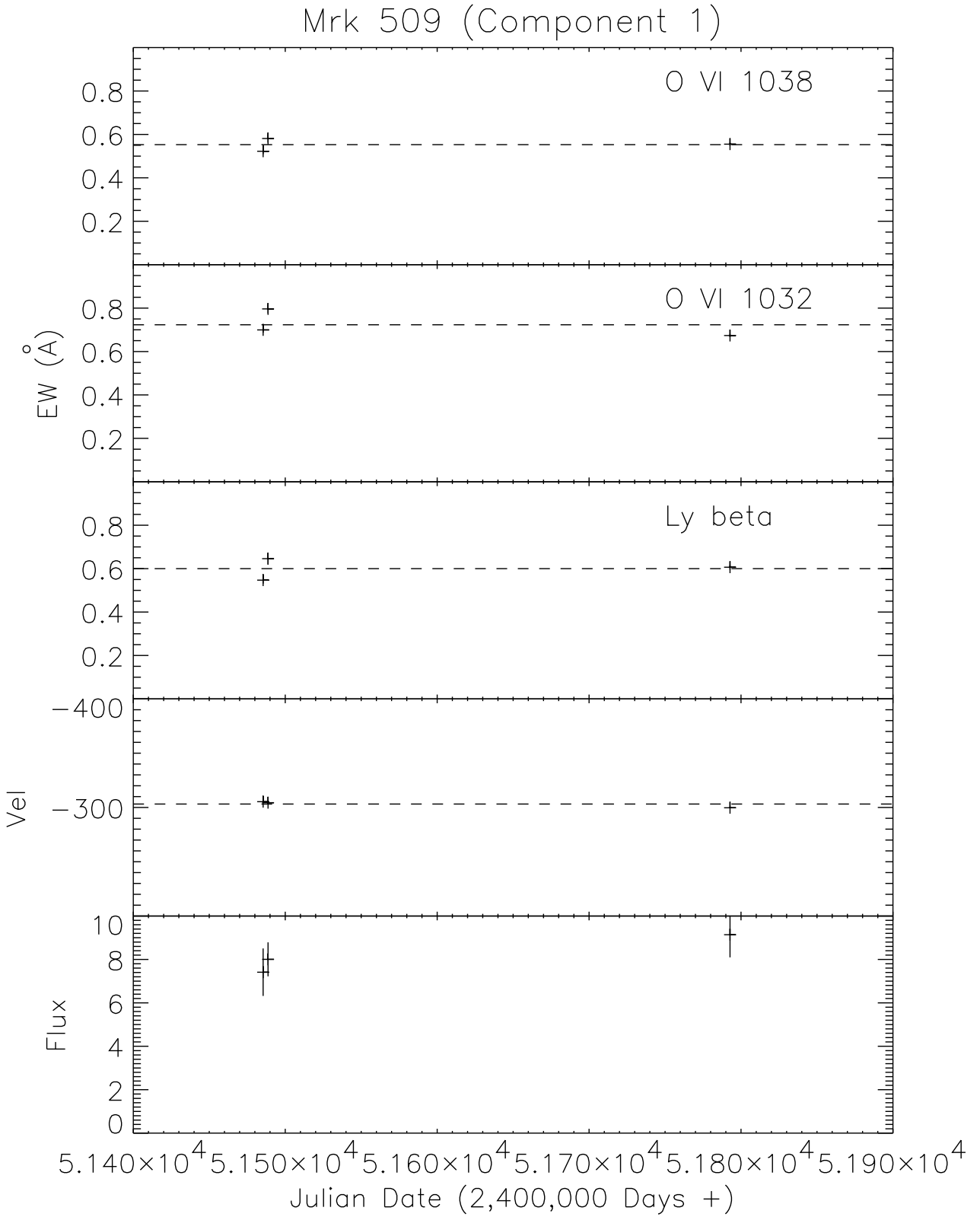


Fig. 17.

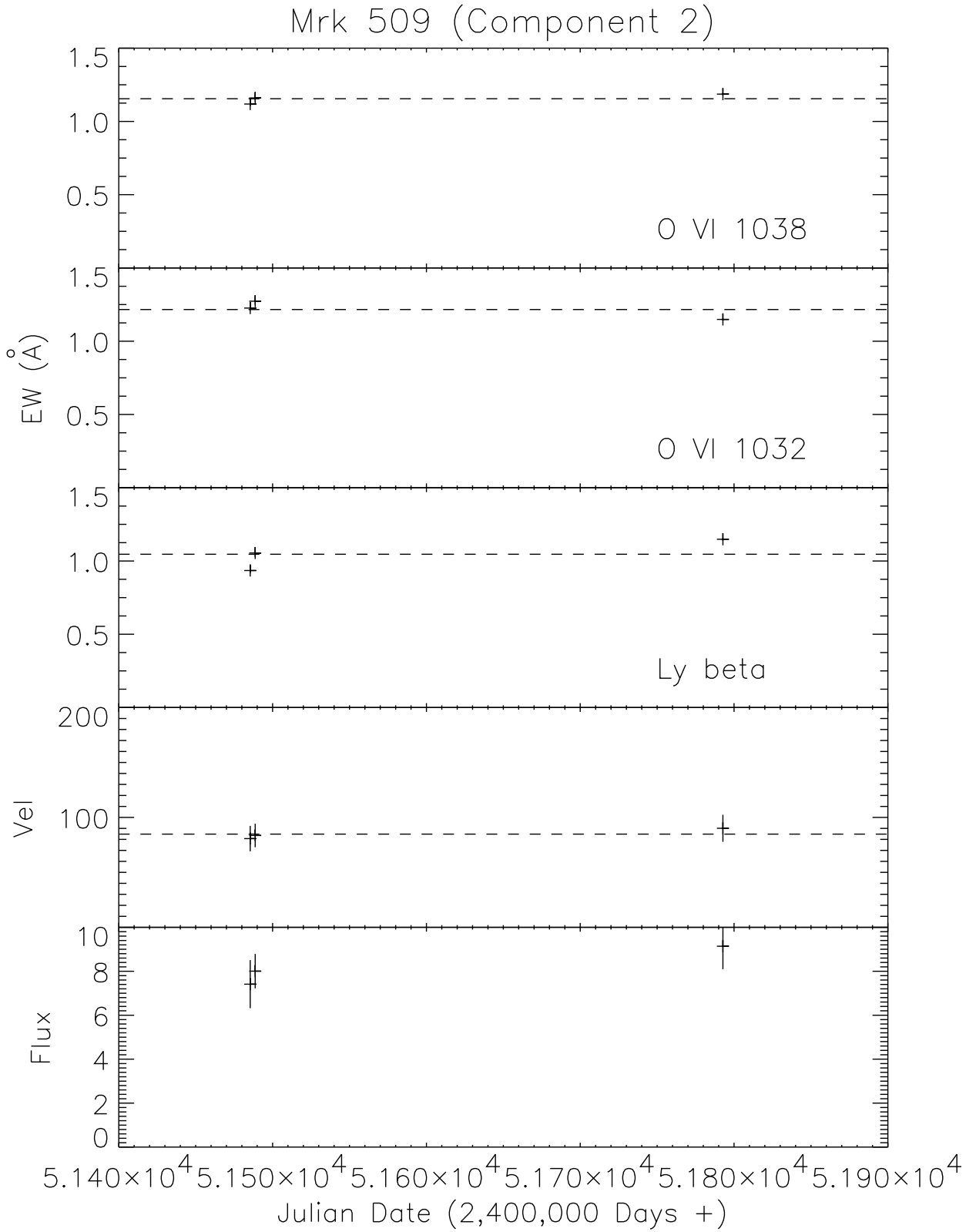


Fig. 18.

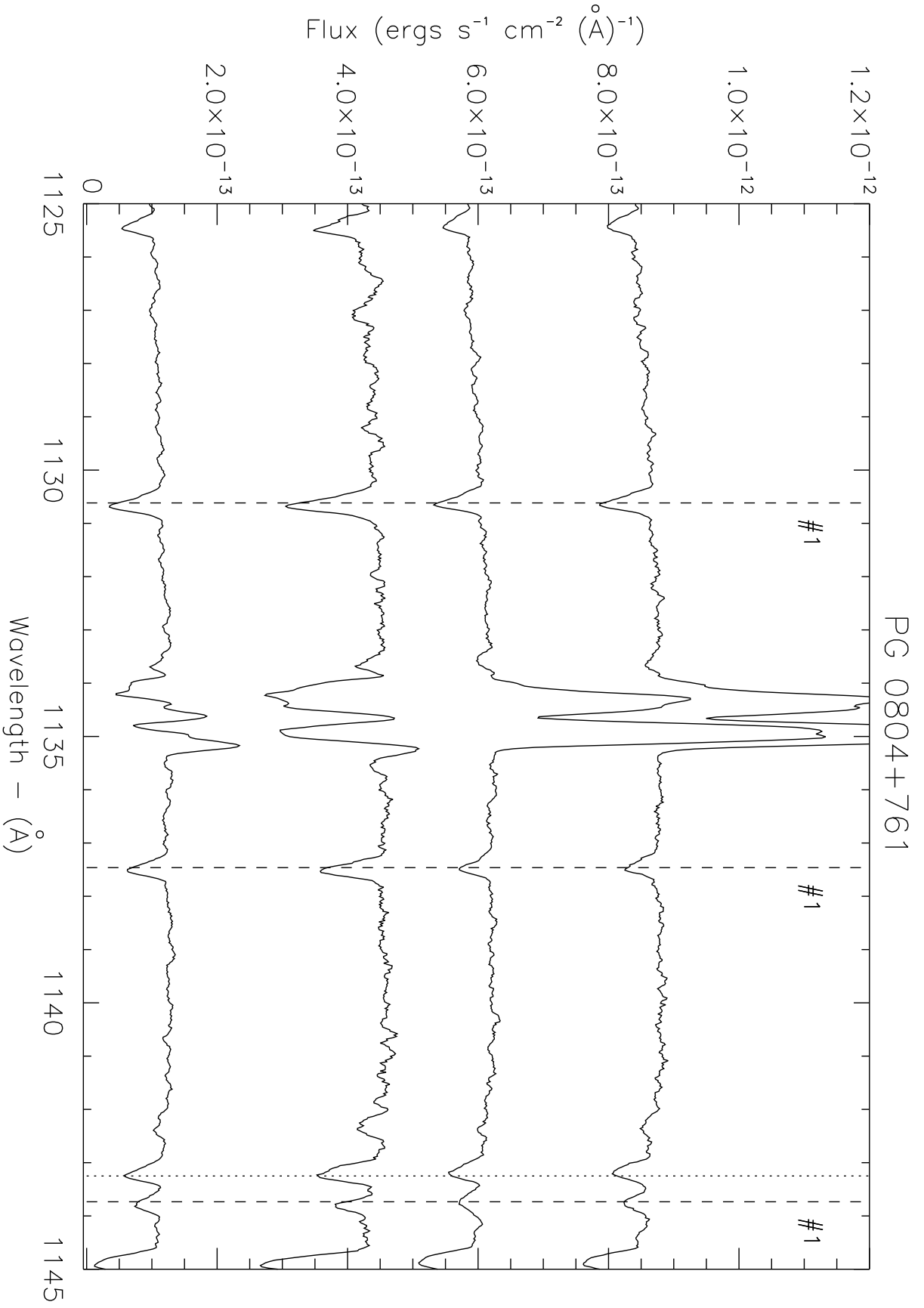


Fig. 19.

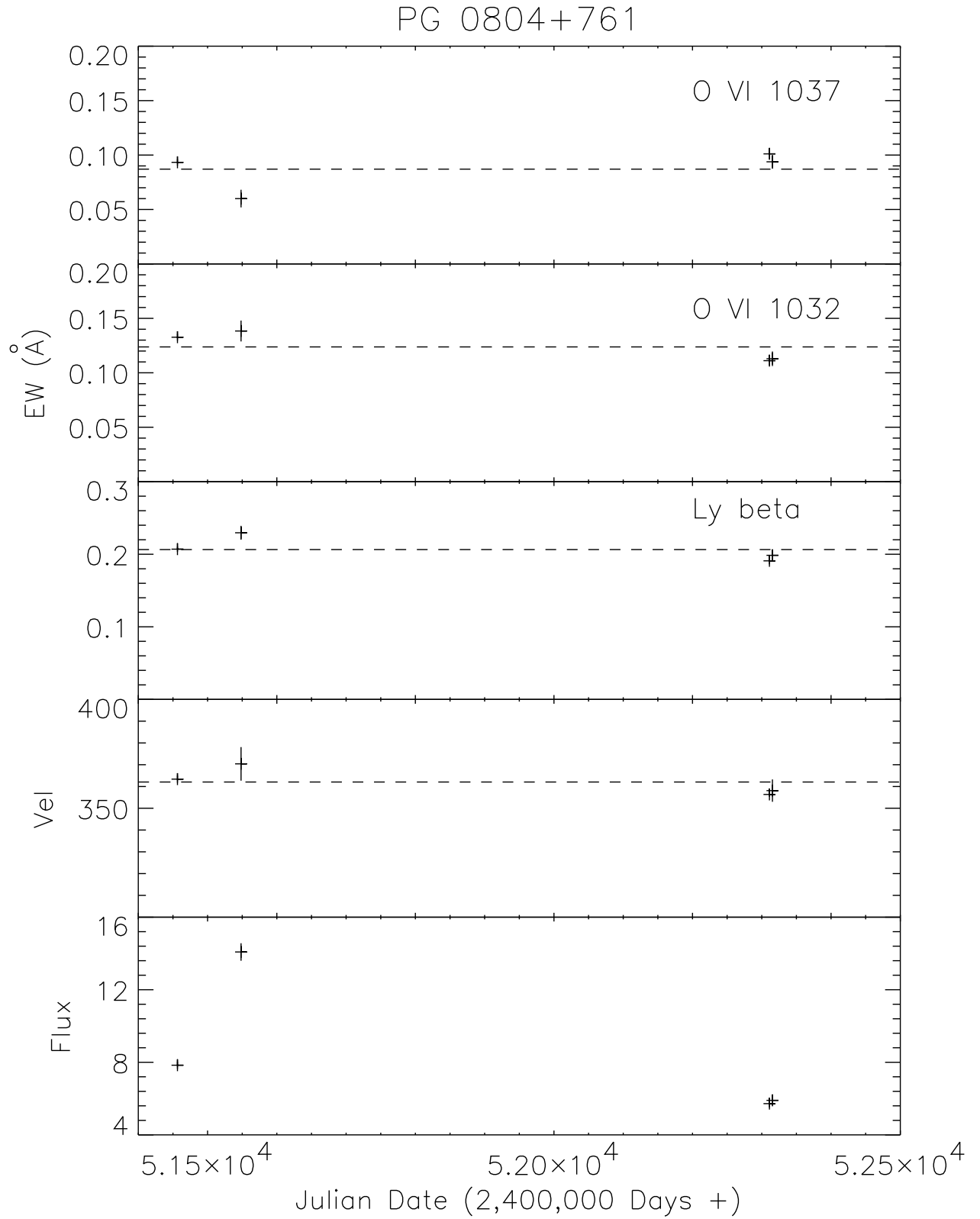


Fig. 20.

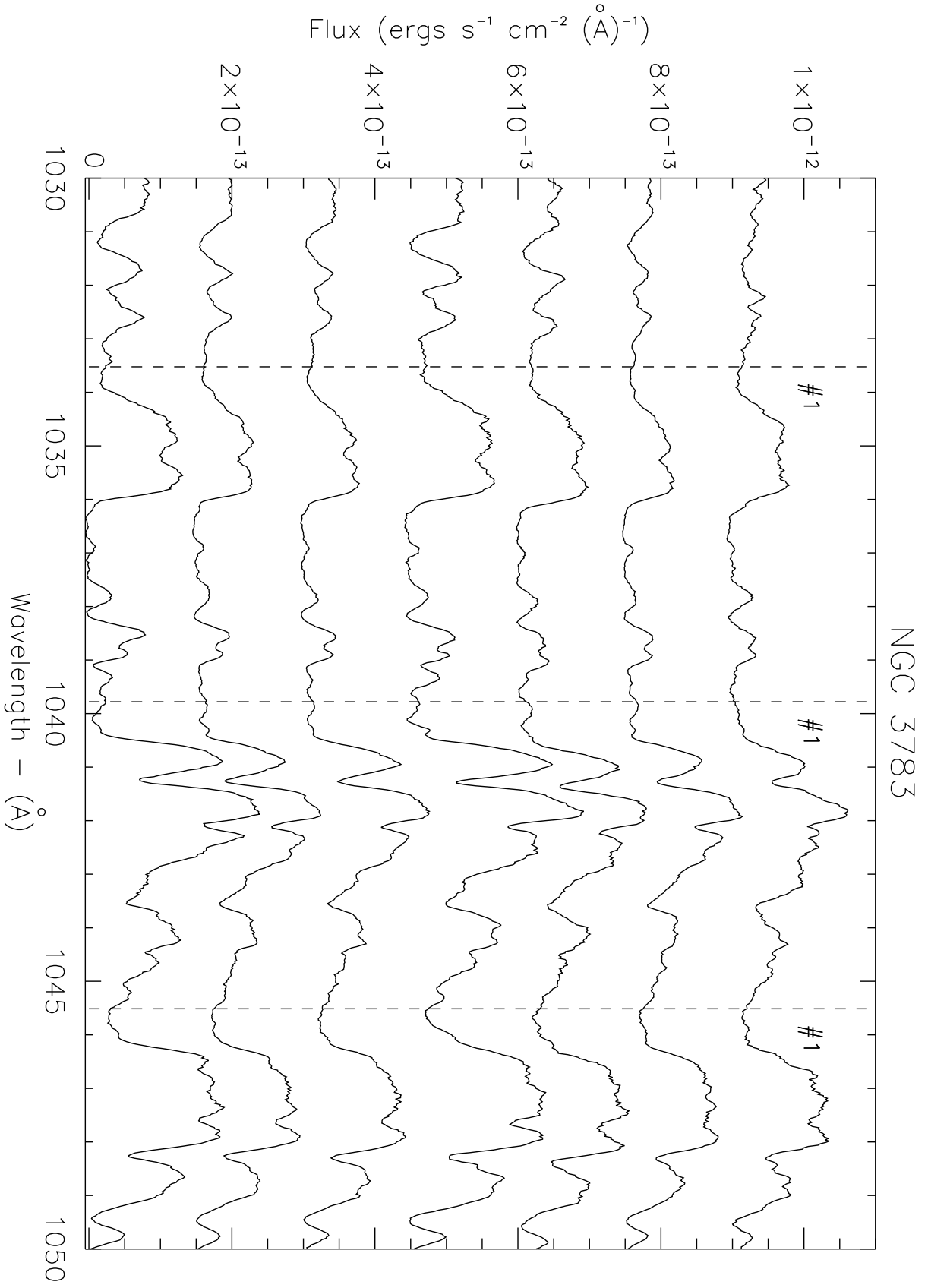


Fig. 21.

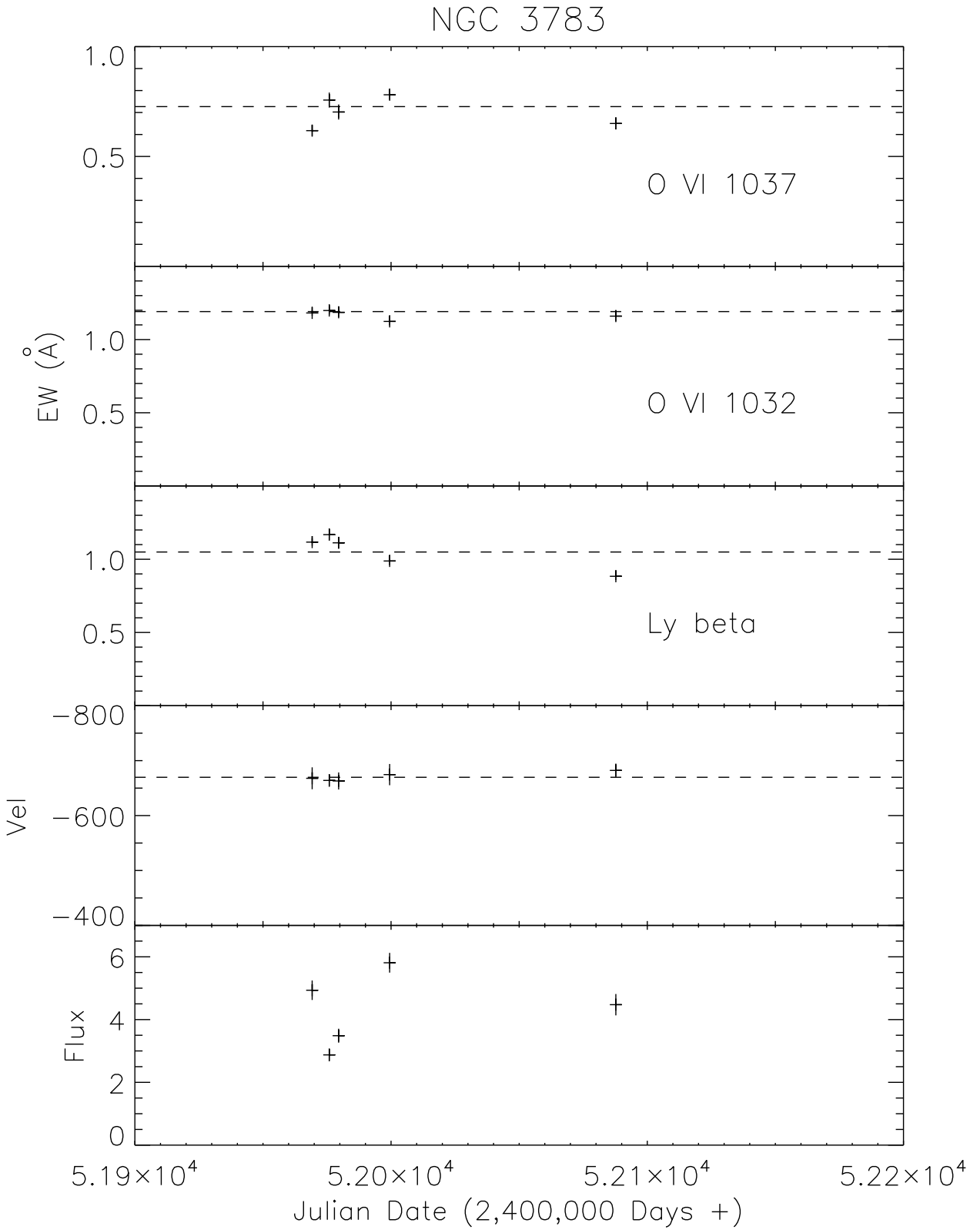


Fig. 22.

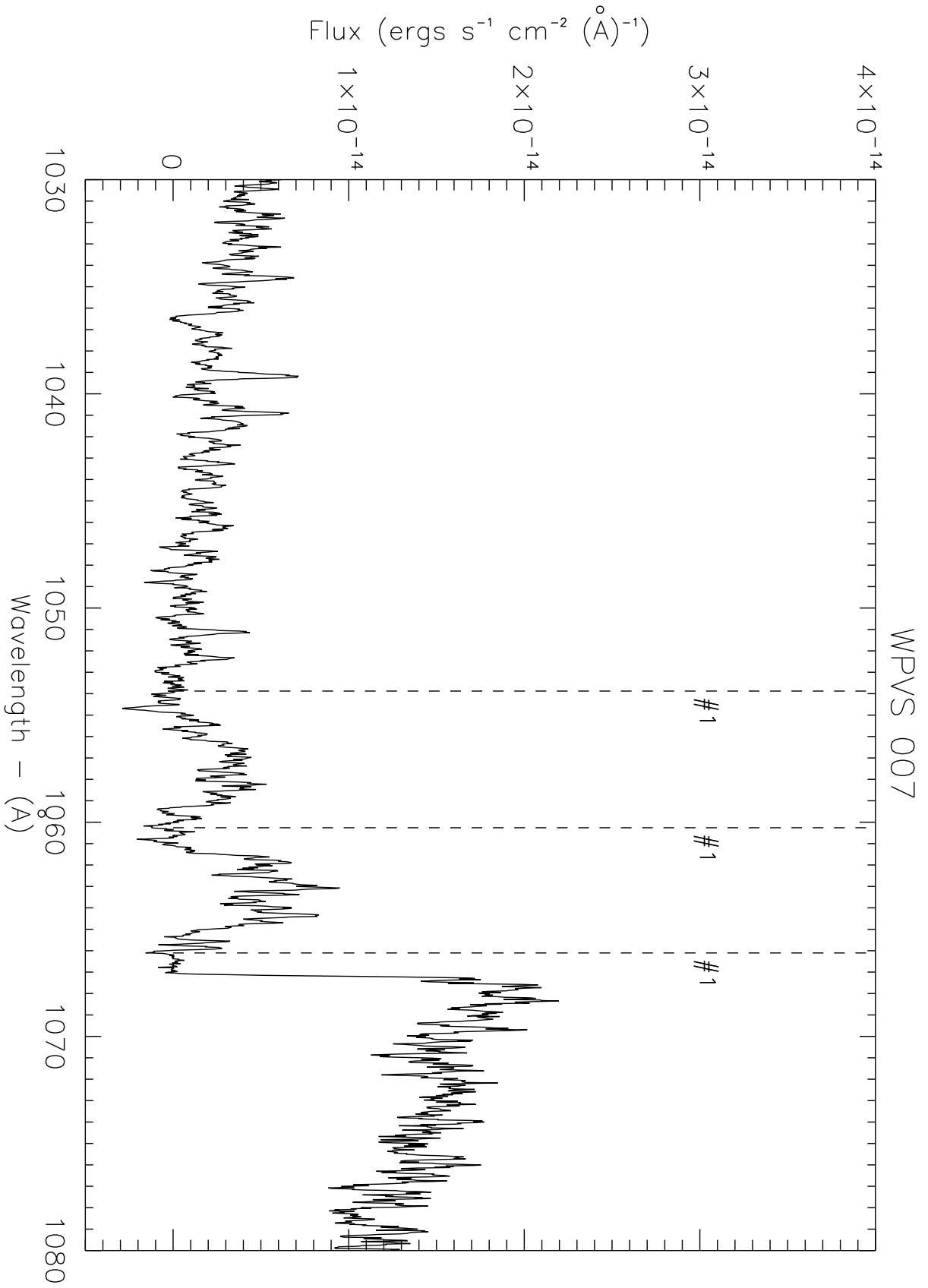


Fig. 23.

Table 1. Observation Log for CTIO Spectra

Object	Date	Integration Time (s)	Resolution FWHM (Å)	λ Coverage (Å)
IRAS F22456-5125	2007 August 9	2400	4.3	3667-5409
IRAS F22456-5125	2007 August 16	2400	3.1	5639-6947
MR 2251-178	2007 August 15	2400	4.3	3667-5423
MR 2251-178	2007 August 17	2400	3.1	5639-6947
WPVS 007	2007 August 15	2400	4.3	3667-5423
WPVS 007	2007 August 17	1800	3.1	5638-6947

Table 2. AGN Continuum Levels

Object	Observation ID	Julian Date +2400000 days	Flux $\times 10^{14}$ ergs s $^{-1}$ Å $^{-1}$	Bin (Å)	Log L $_{\lambda}$ ergs s $^{-1}$ Å $^{-1}$	$\sigma_{LogL_{\lambda}}$ ergs s $^{-1}$ Å $^{-1}$
WPVS 007	D8060201000	52950.360	0.48	1020	39.88	0.11
QSO0045+3926	Z0020401000	51874.176	1.01	1110	41.54	0.03
	D1310101000	52921.336	1.34	1110	41.66	0.05
	D1310102000	52922.707	1.40	1110	41.68	0.05
	D1310103000	52924.391	1.14	1110	41.60	0.04
	D1310104000	52983.242	0.88	1110	41.48	0.06
	D1310105000	53335.281	1.28	1110	41.65	0.07
	D1310106000	53336.105	1.24	1110	41.63	0.07
	D1310107000	53337.000	1.23	1110	41.63	0.07
TONS180	P1010502000	51524.742	6.16	1160	41.66	0.05
	D0280101000	53199.973	4.49	1160	41.52	0.05
MRK1044	D0410101000	53006.246	2.52	1020	40.12	0.09
NGC985	P1010903000	51536.551	2.45	1020	40.94	0.05
EUVEJ0349-537	E8970301000	53237.559	0.36	1110	41.06	0.04
IRASF04250-5718	D8080801000	52886.609	3.66	1110	41.89	0.07
MRK79	P1011701000	51512.949	1.15	1110	40.04	0.11
	P1011702000	51558.152	1.13	1110	40.03	0.10
	P1011703000	51596.613	1.41	1110	40.12	0.08
MRK10	Z9072801000	52673.195	1.07	1110	40.24	0.11
IR07546+3928	S6011801000	52317.062	0.11	1160	40.29	0.08
PG0804+761	P1011901000	51456.504	7.84	1160	42.18	0.01
	P1011903000	54548.312	14.08	1160	42.44	0.02
	S6011001000	52311.059	5.72	1160	42.05	0.02
	S6011002000	52315.406	5.90	1160	42.06	0.02
Ton951	P1012002000	53080.004	4.62	1160	41.56	0.06
	D0280304000	51595.316	3.42	1160	41.43	0.03
	D0280301000	53079.102	2.90	1160	41.36	0.07
IRAS09149-62	A0020503000	51581.129	1.42	1110	40.95	0.04
	S7011003000	53461.098	0.80	1110	40.70	0.09
	U1072202000	53929.031	0.74	1110	40.67	0.06
MKN141	D8061001000	53085.585	0.07	1110	39.09	0.38
NGC3516	P1110404000	51651.957	1.24	1020	38.97	0.18
	G9170101000	53776.217	0.69	1020	38.71	0.20
	G9170102000	54123.776	0.63	1020	38.67	0.23
ESO265-G23	A1210405000	51978.219	0.38	1110	40.36	0.13
	A1210407000	52341.223	0.39	1110	40.37	0.07
	A1210408000	52393.352	0.73	1110	40.64	0.03
	A1210409000	52394.416	1.03	1110	40.79	0.04
NGC3783	P1013301000	51576.621	4.90	1160	39.95	0.03
	B1070102000	51969.199	4.94	1160	39.95	0.03
	B1070103000	51979.535	3.49	1160	39.80	0.03
	B1070104000	51999.453	5.81	1160	40.02	0.03
	B1070105000	52087.727	4.47	1160	39.91	0.04

Table 2—Continued

Object	Observation ID	Julian Date +2400000 days	Flux $\times 10^{14}$ ergs $s^{-1} \text{ \AA}^{-1}$	Bin (\AA)	Log L_{λ} ergs $s^{-1} \text{ \AA}^{-1}$	$\sigma_{\text{Log}L_{\lambda}}$ ergs $s^{-1} \text{ \AA}^{-1}$
	B1070106000	51975.855	2.87	1160	39.72	0.03
	E0310101000	53130.965	4.11	1160	39.87	0.03
NGC4051	B0620201000	52362.582	1.29	1020	38.13	0.05
	C0190101000	52657.988	1.35	1020	38.15	0.07
	C0190102000	52717.824	1.51	1020	38.20	0.07
NGC4151	P1110505000	51609.410	2.50	1020	38.72	0.05
	P2110201000	52008.199	1.71	1020	38.56	0.08
	C0920101000	52423.469	21.52	1020	39.66	0.03
	P2110202000	52427.199	12.67	1020	39.43	0.05
RXJ1230.8+0115	P1019001000	51715.832	5.24	1110	42.14	0.06
TOL1238-364	D0100101000	51945.742	1.47	1110	39.53	0.06
PG1351+640	P1072501000	51562.117	1.19	1160	41.25	0.03
	S6010701000	52306.922	1.68	1160	41.40	0.02
MRK279	P1080303000	51540.527	11.45	1110	41.31	0.01
	P1080304000	51554.562	9.61	1110	41.23	0.02
	C0900201000	52413.258	0.61	1110	40.04	0.02
	D1540101000	52772.410	9.20	1110	41.21	0.01
	F3250103000	53711.961	7.35	1110	41.12	0.02
	F3250104000	53713.277	2.86	1110	40.70	0.08
	F3250106000	53769.598	4.53	1110	40.90	0.05
RXJ135515+561244	D8061601000	52712.387	0.39	1110	41.04	0.02
PG1404+226	P2100401000	52071.652	0.93	1110	41.23	0.10
PG1411+442	A0601010000	51675.637	2.01	1160	41.49	0.06
NGC5548	P1014601000	51703.055	1.55	1020	39.94	0.05
MRK817	P1080401000	51591.965	9.05	1110	41.23	0.03
	P1080402000	51592.766	7.20	1110	41.13	0.03
	P1080403000	51902.176	3.89	1110	40.87	0.003
	P1080404000	51958.891	6.25	1110	41.07	0.01
MRK290	P1072901000	51620.230	0.45	1110	39.87	0.08
	D0760101000	52819.457	3.44	1110	40.76	0.06
	E0840101000	53171.730	3.83	1110	40.81	0.06
MRK876	P1073101000	51467.766	0.24	1110	40.88	0.03
	D0280201000	52776.450	5.77	1110	42.26	0.08
	D0280203000	53049.797	5.71	1110	42.26	0.03
MRK509	X0170101000	51485.445	7.41	1020	41.23	0.05
	X0170102000	51488.703	8.00	1020	41.26	0.06
	P1080601000	51792.750	9.14	1020	41.32	0.05
IIZW136	P1018301000	51863.473	2.36	1160	41.25	0.04
	P1018302000	53152.684	3.72	1160	41.45	0.07
	P1018303000	53153.727	2.79	1160	41.33	0.07
	P1018304000	53310.586	3.71	1160	41.45	0.04
AKN564	B0620101000	52089.816	1.03	1110	40.08	0.02
IRAS F22456-5125	Z9073901000	52541.902	1.12	1110	41.33	0.10

Table 2—Continued

Object	Observation ID	Julian Date +2400000 days	Flux $\times 10^{14}$ ergs s ⁻¹ Å ⁻¹	Bin (Å)	Log L _λ ergs s ⁻¹ Å ⁻¹	σ_{LogL_λ} ergs s ⁻¹ Å ⁻¹
	Z9073902000	52542.457	1.75	1110	41.52	0.04
	E8481401000	53194.629	6.08	1110	42.07	0.08
MR 2251-178	P1111010000	52081.012	0.99	1160	40.89	0.04
NGC7469	P1074101000	51724.101	1.30	1020	39.52	0.08
	C0900101000	52621.797	2.11	1020	39.73	0.14
	C0900102000	52621.767	2.17	1020	39.74	0.15

Table 3. Measured Quantities

Object	Obs ID	Comp	Equivalent Width			σ_{EW}			FWHM			V_r (km s ⁻¹)	σ_{vel} (km s ⁻¹)
			Ly β (Å)	O VIb (Å)	O VIr (Å)	Ly β (Å)	O VIb (Å)	O VIr (Å)	Ly β	O VIb (km s ⁻¹)	O VIr		
WPVS 007	D8060201000	1	1.91	2.06	1.76	0.14	0.13	0.14	714	639	615	-397	26
QSO0045+3926	Z0020401000	1	0.29	0.61	0.29	0.04	0.06	0.05	100	172	69	361	13
	D1310101000	1	0.19	0.45	0.38	0.01	0.01	0.01	56	128	98	351	5
	D1310102000	1	0.19	0.38	0.29	0.02	0.02	0.02	69	101	107	345	12
	D1310103000	1	0.29	0.41	0.27	0.08	0.06	0.06	77	121	63	340	22
	D1310104000	1	0.17	0.36	0.31	0.01	0.02	0.02	82	107	74	346	16
	D1310105000	1	0.13	0.40	0.33	0.02	0.02	0.02	86	107	94	371	6
	D1310106000	1	0.16	0.42	0.28	0.02	0.02	0.02	69	91	85	375	7
	D1310107000	1	0.14	0.33	0.32	0.02	0.03	0.02	60	77	73	396	9
TONS180	P1010502000	1			0.13			0.03			65	-1732	
	D0280101000	1			0.17			0.03			85	-1792	
MRK1044	D0410101000	1	0.20	0.22		0.04	0.03		65	92		-1110	2
NGC985	P1010903000	1		0.11	0.06		0.01	0.01		96	77	-814	20
	P1010903000	2	0.12	0.26	0.20	0.02	0.01	0.01	34	72	55	-678	6
	P1010903000	3	0.56	0.71	0.65	0.02	0.02	0.01	158	199	180	-454	51
	P1010903000	4	0.15	0.16	0.23	0.02	0.01	0.01	41	44	63	-268	17
EUVEJ0349-537	E8970301000	1	0.47	0.71	0.60	0.04	0.04	0.06	128	218	165	26	21
IRASF04250-5718	D8080801000	1	0.56	0.62	0.64	0.06	0.07	0.07	159	195	184	-216	5
	D8080801000	2	0.15	0.25	0.20	0.06	0.03	0.03	41	66	51	-64	2
MRK79	P1011701000	1	0.35	0.65	0.76	0.18	0.17	0.17	117	242	220	-350	12
	P1011702000	1	0.30	0.52	0.43	0.10	0.09	0.08	175	240	160	-325	35
	P1011703000	1	0.18	0.57	0.52	0.07	0.08	0.06	86	198	194	-326	27
	P1011701000	2			0.39			0.13			255	-1404	
	P1011702000	2			0.31			0.08			87	-1387	
MRK10	Z9072801000	2			0.28			0.07		81	-1367		
MRK10	Z9072801000	1	1.03		0.92	0.09		0.13	344		227	-126	18
	IR07546+3928	S6011801000	1	1.07	1.49	1.00	0.05	0.03	0.02	280	436	351	-1777
PG0804+761	S6011801000	2	0.98	1.48	1.37	0.03	0.03	0.03	263	395	361	-1116	12
	P1011901000	1	0.21	0.13	0.09	0.004	0.003	0.003	69	67	64	363	7
PG0804+761	P1011903000	1	0.23	0.14	0.06	0.01	0.01	0.01	75	66	55	370	2
	S6011001000	1	0.19	0.11	0.10	0.01	0.004	0.01	63	64	81	356	1
	S6011002000	1	0.20	0.11	0.09	0.01	0.01	0.01	74	66	71	358	5

Table 3—Continued

Object	Obs ID	Comp	Equivalent Width			σ_{EW}			FWHM			V_r (km s ⁻¹)	σ_{vel} (km s ⁻¹)
			Ly β (Å)	O VIb (Å)	O VIr (Å)	Ly β (Å)	O VIb (Å)	O VIr (Å)	Ly β	O VIb (km s ⁻¹)	O VIr		
TON951	P1012002000	1	0.60	0.43	0.43	0.02	0.01	0.01	159	123	118	179	16
	D0280304000	1	0.69	0.42	0.46	0.05	0.03	0.02	190	150	128	173	25
	D0280301000	1	0.66	0.52	0.41	0.05	0.05	0.02	186	149	114	149	23
IRAS09149-62	A0020503000	1		1.72	1.26			0.22		504	389	18	18
	S7011003000	1			1.08			0.11			377	31	
	U1072202000	1			1.33			0.08			431	56	
NGC3516	P1110404000	1	0.27	1.76	0.06	0.07	0.09	0.03	168	510	52	-1511	360
	G9170101000	1	0.33	1.40	0.14	0.13	0.17	0.20	177	468	133	-1362	6.8
	G9170102000	1	0.23	0.53	0.15	0.07	0.07	0.04	133	202	63	-1343	101
	P1110404000	2		0.54	0.08			0.06		250	162	-866	125
	G9170101000	2	0.38	0.57	0.64	0.16	0.12	0.20	212	239	331	-888	38
	G9170102000	2	0.15	0.28	0.34	0.06	0.05	0.05	112	99	198	-911	52
	P1110404000	3		0.28	0.35			0.04		123	46	-410	15
	G9170101000	3	0.38		0.58	0.15		0.12	168		196	-460	10
	G9170102000	3	0.34	0.32	0.38	0.06	0.06	0.05	113	98	100	-456	2
	P1110404000	4	0.38	0.38	0.40	0.08	0.05	0.06	110	163	239	-216	1
	G9170101000	4	0.58		0.46	0.17		0.23	226		174	-236	30
	G9170102000	4	0.67	0.79	0.80	0.06	0.06	0.07	233	287	302	-227	6
ESO265-G23	A1210405000	1		0.29	0.15			0.15		127	126	-178	13
	A1210407000	1		0.34	0.32			0.05		141	73	-157	5
	A1210408000	1		0.29	0.36			0.10		63	288	-124	14
	A1210409000	1		0.34	0.30			0.13		92	81	-157	26
NGC3783	P1013301000	1	1.03	1.19	0.78	0.02	0.02	0.03	403	463	404	-660	10
	B1070102000	1	1.12	1.18	0.62	0.03	0.02	0.03	394	467	456	-668	20
	B1070103000	1	1.11	1.19	0.70	0.04	0.03	0.03	400	452	449	-663	16
	B1070104000	1	0.99	1.12	0.78	0.03	0.03	0.02	332	443	393	-675	19
	B1070105000	1	0.88	1.16	0.65	0.03	0.03	0.03	377	459	404	-682	13
	B1070106000	1	1.17	1.20	0.76	0.04	0.03	0.03	427	457	395	-664	12
	E0310101000	1	1.05	1.30	0.80	0.02	0.03	0.02	380	467	371	-657	30
NGC4051	B0620201000	1		2.28				0.00		672		-374	
	C0190101000	1		2.13				0.04		696		-348	
	C0190102000	1		2.14	1.88			0.05	0.04	670	627	-359	12

Table 3—Continued

Object	Obs ID	Comp	Equivalent Width			σ_{EW}			FWHM			V_r (km s ⁻¹)	σ_{vel} (km s ⁻¹)	
			Ly β (Å)	O VIb (Å)	O VIr (Å)	Ly β (Å)	O VIb (Å)	O VIr (Å)	Ly β	O VIb (km s ⁻¹)	O VIr			
NGC4151	P1110505000	1		0.91			0.04				473		-706	
	P2110201000	1		1.48	1.21		0.07	0.04			514	522	-574	222
	C0920101000	1		1.77	1.95		0.01	0.01			718	681	-397	41
RXJ1230.8+0115	P2110202000	1		1.66	1.99		0.08	0.05			662	716	-413	56
	P1019001000	1		1.90	1.57		0.09	0.08			542	476	-2994	16
	P1019001000	2		0.27	0.26		0.06	0.05			71	69	-2420	50
	P1019001000	3		1.19	1.07		0.08	0.06			311	278	-2014	3
	P1019001000	4		1.17	1.08		0.06	0.08			304	280	120	2
TOL1238-364	D0100101000	1		1.10	1.51		0.14	0.15			339	454	-252	75
PG1351+640	P1072501000	1	0.60	1.31	1.20	0.01	0.01	0.01	182	453	447		-1705	73
	S6010701000	1	0.54	1.37	1.42	0.02	0.02	0.02	208	455	429		-1715	60
	P1072501000	2	1.51	2.08	1.94	0.02	0.01	0.01	407	559	516		-883	24
	S6010701000	2	1.23	2.16	2.12	0.02	0.02	0.02	333	579	565		-899	11
MRK279	P1080303000	1	0.77	1.20	0.75	0.01	0.01	0.01	321	478	301		-312	6
	P1080304000	1	0.82	1.15	0.77	0.02	0.02	0.02	328	482	307		-328	4
	C0900201000	1	1.01	0.96	1.06	0.07	0.06	0.06	299	497	312		-351	2
	D1540101000	1	0.76	1.32	0.97	0.01	0.01	0.01	290	474	319		-308	8
	F3250103000	1	1.19	1.80	0.97	0.13	0.10	0.10	285	508	306		-404	33
	F3250104000	1	0.87	1.64	0.93	0.13	0.13	0.11	392	518	366		-302	12
	F3250106000	1	0.69	1.26	0.90	0.22	0.21	0.16	324	502	328		-308	28
	D8061601000	1	0.34	0.61	0.76	0.04	0.04	0.05	86	160	205		-834	12
RXJ135515+561244	D8061601000	2		0.69	0.48		0.05	0.03			180	186	-163	28
	P2100401000	1	0.19	0.54	0.36	0.04	0.03	0.04	88	151	127		-166	57
PG1404+226	P2100401000	2		1.47	1.11		0.06	0.07			330	284	134	17
	A0601010000	1			0.64			0.03				170	55	
PG1411+442	P1014601000	1		0.35	0.25		0.02	0.02			161	195	-441	4
	P1014601000	2		0.25	0.31		0.02	0.02			111	142	-683	5
MRK817	P1080401000	1	0.08	0.60	0.41	0.05	0.04	0.05	319	207	143		-4198	5
	P1080402000	1	0.12	0.51	0.39	0.05	0.05	0.06	236	237	146		-4184	16
	P1080403000	1	0.10	0.41	0.36	0.01	0.02	0.02	134	273	265		-4166	32
	P1080404000	1	0.06	0.40	0.33	0.01	0.00	0.01	210	208	154		-4144	12
	P1080404000	2		0.12	0.05		0.01	0.01			243	142	-3680	27

Table 3—Continued

Object	Obs ID	Comp	Equivalent Width			σ_{EW}			FWHM			V_r (km s ⁻¹)	σ_{vel} (km s ⁻¹)
			$L_{y\beta}$ (Å)	O VIb (Å)	O VIr (Å)	$L_{y\beta}$ (Å)	O VIb (Å)	O VIr (Å)	$L_{y\beta}$	O VIb (km s ⁻¹)	O VIr		
	P1080404000	3		0.12	0.09		0.01	0.01		118	139	-2966	6
MRK290	P1072901000	1	0.71	0.62	0.54	0.12	0.10	0.08	185	190	142	-225	14
	D0760101000	1	0.51	0.59	0.48	0.07	0.05	0.05	141	192	165	-212	17
	E0840101000	1	0.54	0.48	0.43	0.05	0.05	0.05	180	157	158	-187	72
MRK876	P1073101000	1		0.11	0.09		0.01	0.01		73	99	-3735	3
	D0280203000	1		0.15	0.11		0.00	0.00		101	94	-3724	0.8
MRK509	X0170101000	1	0.55	0.70	0.52	0.02	0.01	0.01	217	217	182	-305	16
	X0170102000	1	0.65	0.80	0.58	0.03	0.02	0.02	218	204	190	-304	19
	P1080601000	1	0.61	0.67	0.56	0.01	0.01	0.01	170	201	177	-300	18
	X0170101000	2	0.95	1.23	1.12	0.02	0.01	0.01	303	329	346	103	12
	X0170102000	2	1.05	1.27	1.16	0.03	0.02	0.03	321	331	322	27	11
	P1080601000	2	1.15	1.15	1.19	0.01	0.01	0.01	330	333	341	90	12
IIZW136	P1018301000	1		0.42			0.02			146		-1487	
	P1018302000	1		0.47			0.03			173		-1512	
	P1018303000	1		0.49			0.04			96		-1517	
	P1018304000	1		0.45			0.03			167		-1512	
	P1018301000	2			0.28			0.02			87	9	
	P1018302000	2			0.30			0.04			96	-2	
	P1018303000	2			0.18			0.03			61	9	
	P1018304000	2			0.31			0.02			99	-7	
AKN564	B0620101000	1	1.64	1.28	1.31	0.04	0.02	0.03	528	304	280	-65	10
IRAS F22456-5125	Z9073901000	1	0.06	0.32	0.28	0.04	0.06	0.06	42	110	105	-787	11
	Z9073902000	1	0.07	0.19	0.17	0.01	0.01	0.01	81	64	69	-803	22
	E8481401000	1	0.06	0.24	0.29	0.05	0.04	0.07	50	73	99	-812	28
	Z9073901000	2	0.42			0.05			130			-596	
	Z9073902000	2	0.35			0.01			97			-612	
	E8481401000	2	0.44			0.06			110			-617	
	Z9073901000	3	0.38	0.23	0.25	0.06	0.05	0.05	117	66	101	-424	9
	Z9073902000	3	0.27	0.20	0.21	0.01	0.01	0.01	77	67	69	-455	5
	E8481401000	3	0.33	0.38	0.26	0.05	0.06	0.06	96	151	94	-447	13
	Z9073901000	4	0.09	0.17	0.10	0.05	0.05	0.04	56	66	42	-311	3
	Z9073902000	4	0.08	0.21	0.14	0.01	0.01	0.01	40	63	66	-323	5

Table 3—Continued

Object	Obs ID	Comp	Equivalent Width			σ_{EW}			FWHM			V_r (km s ⁻¹)	σ_{vel} (km s ⁻¹)
			Ly β (Å)	O VIb (Å)	O VIr (Å)	Ly β (Å)	O VIb (Å)	O VIr (Å)	Ly β	O VIb (km s ⁻¹)	O VIr		
	E8481401000	4	0.12	0.18	0.14	0.05	0.05	0.04	35	105	39	-327	1
	Z9073901000	5	0.70	0.51	0.54	0.08	0.06	0.07	190	142	143	-118	19
	Z9073902000	5	0.68	0.67	0.46	0.01	0.01	0.01	182	136	134	-135	22
	E8481401000	5	0.72	0.54	0.57	0.07	0.06	0.07	178	147	137	-136	21
MR 2251-178	P1111010000	1	1.62	0.70	0.40	0.03	0.01	0.01	418	234	155	-300	23
NGC7469	C0900101000	1		0.40	0.30		0.002	0.01		151	137	-1847	17
	C0900102000	1		0.48	0.40		0.01	0.01		209	190	-1878	3

Table 4. Central Black Hole Masses

Object	FWHM H β km s $^{-1}$	Mass $\times 10^6$	log λL_λ ergs s $^{-1}$	log L_{Bol} ergs s $^{-1}$	L/ L_{Edd}	reference ^b
Mrk 79		52.4	43.72	44.71	0.08	1
PG 0804+761		693	44.94	45.93	0.10	1
NGC 3516		42.7	42.88	43.87	0.01	1
NGC 3783		29.8	43.26	44.25	0.05	1
NGC 4051		1.91	41.93	42.92	0.03	1
NGC 4151		13.3	42.88	43.87	0.04	1
Mrk 279		34.9	43.88	44.87	0.17	1
PG 1411+422		443	44.63	45.62	0.07	1
NGC5548		67.1	43.51	44.50	0.04	1
Mrk 817		49.4	43.82	44.81	0.10	1
Mrk 509		143	44.28	45.27	0.10	1
NGC 7469		12.2	43.72	44.71	0.33	1
Mrk 876		279	44.98	45.97	0.27	1
Ton 951		92.4	44.35	45.34	0.19	1
II Zw 136		457	44.46	45.45	0.05	1
PG 1351+640	1170	46	44.64	45.63	0.74	2
QSO 0045+3926	5970	564.9	44.60	45.59	0.05	7
Ton S180	970	10.2	44.27	45.26	1.42	3
NGC 985	5670	202.8	43.80	44.79	0.02	3
IRAS F04250-5718	2580	144.0	44.87	45.86	0.40	3
Mrk 10	3050	25.6	43.08	44.07	0.04	4
IR 07546+3928	2120	176.9	45.39 ^a	46.39	1.10	8
Mrk 141	3600	65.0	43.60	44.59	0.05	3
RXJ 135515+561244	1100	9.4	43.98	44.97	0.79	3
PG 1404+226	790	7.7	44.38	44.37	2.43	5
Mrk 290	5320	157.3	43.69	44.68	0.02	5
Akn 564	970	4.8	43.62	44.61	0.67	4
MR 2251-5125	3768	240.0	44.64	45.63	0.14	6
IRAS F22456-5125	3297	154.9	42.76 ^a	45.53	0.16	6
WPVS 007	1502	11.5	43.59	44.58	0.27	6
RXJ 1230.8+0115				45.0	0.13	9

^aMass calculated from H β luminosity

^b1-Peterson et al. 2004, 2-Kaspi et al. 2000, 3-Grupe et al. 2004, 4-Botte et al. 2004,

5-Vestergaard et al. 2006 6-This Paper, 7-Xu et al. 2003, 8-Marziani et al. 2003, 9-Ganguly et al. 2003

$$c_{Bol} = 9.8 \lambda L_{5100}$$